MetalMat

WILEY

MetalMat
ALL ABOUT METALS IN SCIENCE AND TECHNOLOGY Open Access

REVIEW OPEN ACCESS

Low-Temperature Thermochemical Treatments of Face-Centered Cubic Alloys: New Perspectives for Expanded Austenite From Austenitic Stainless Steels to High-Entropy Alloys

Francesca Borgioli

Department of Industrial Engineering (DIEF), University of Florence, Florence, Italy

Correspondence: Francesca Borgioli (francesca.borgioli@unifi.it)

Received: 30 April 2025 | **Revised:** 11 July 2025 | **Accepted:** 16 July 2025

Funding: The author received no specific funding for this work.

Keywords: austenitic stainless steels | Co alloys | entropy alloys | expanded austenite | low-temperature thermochemical treatments | Ni alloys | S-phase

ABSTRACT

Thermochemical treatments performed at low temperatures (< ~500°C) have received increasing interest for the surface modification of austenitic stainless steels. In fact, when treatment media rich in nitrogen and/or carbon are used at these temperatures, the formation of chromium compounds is inhibited and the interstitial atoms are retained in the face-centered cubic lattice of austenite beyond the solubility limit. The obtained supersaturated solid solution, known as expanded austenite or S-phase, has high hardness and can maintain or even increase the corrosion resistance in many environments. In the international literature, many studies are present that highlight the effects of the formation of this phase on tribological properties, fatigue resistance, corrosion behavior, wettability, biocompatibility, and magnetic properties of austenitic stainless steels. However, using analogous treatment conditions, expanded austenite can be obtained in many other alloys having a matrix with a face-centered cubic lattice, such as austenitic steels, nickel and cobalt alloys, and the more recent medium- and high-entropy alloys, but the studies on this topic are mostly at their very beginning. In this review, the characteristics and properties of expanded austenite and of the modified surface layers in which it is present are analyzed and discussed, considering all the different alloys in which this supersaturated phase can be produced. The role of alloy elements in promoting or hindering the formation of expanded austenite and the competing compound precipitates is taken into account. The opportunities and challenges of the low-temperature treatments are highlighted, and possible future directions for the investigation are suggested.

1 | Introduction

Surface engineering has become an important step in the industrial manufacturing of metal alloys. By modifying the topmost part of the material, it is possible to improve the surface hardness, tribological properties, corrosion resistance, biocompatibility, or simply change the esthetic appearance of a component, while maintaining the mechanical and physical characteristics of the bulk alloy [1–3]. The surface modification can be obtained using different strategies. More or less thick coatings can be deposited by means of processes such as plating, chemical vapor deposition (CVD), physical vapor deposition (PVD), or plasma spray [1, 2]. Another approach consists in modifying the outer part of the material by means of the diffusion of interstitial atoms or metal atoms using thermochemical treatments, such as nitriding, carburizing, boriding or aluminizing [1, 3].

The surface alloying with nitrogen (N) and/or carbon (C) is a well-consolidated practice for the surface hardening of steels. On low-alloy steels and tool steels, nitriding treatments (T = 500–580°C) produce an outer nitride layer, known as compound layer or white layer, and an inner diffusion layer, in which nitride precipitates are dispersed in a solid solution of N in the ferrite matrix [3, 4]. Using carburizing (T = 850–950°C), the C enrichment in the austenite field and the subsequent quenching and tempering produce a modified layer consisting of tempered martensite with dispersed carbide precipitates and eventual retained austenite [3, 5]. However, the compounds (nitrides/carbides) formed in conventional treatments may have adverse effects on the performance of some alloy grades. As an example, in stainless steels these treatments cause the precipitation of chromium (Cr) compounds, so that the Cr-depleted matrix cannot form a protective passive film and hence the corrosion resistance is worsened [6]. For stainless steels more suitable surface treatments are the so-called low-temperature thermochemical treatments [7]. By using treatment temperatures usually in the range 300–500°C, N and C atoms can diffuse freely in the lattice, although the diffusion of substitutional atoms (e.g., Cr) is significantly slowed down. Consequently, the formation of Cr compounds is inhibited and corrosion resistance can be preserved. In these para-equilibrium conditions [8], interstitial atoms are retained in the metal lattice and a supersaturated solid solution forms, which may have an interstitial content up to several hundred times higher than equilibrium solubility [9]. These so-called "expanded" phases can be obtained in all the iron (Fe)-based lattice structures, that is, face-centered cubic (fcc) austenite, body-centered cubic (bcc) ferrite and body-centered tetragonal (bct) martensite, and hence in all the stainless steel grades, and they allow for a significant improvement in surface hardness [9, 10].

Most of the studies on low-temperature thermochemical treatments concern austenitic stainless steels and expanded austenite, due to the interesting characteristics of the modified surface layers [11]. Thanks to the increase in surface hardness, tribological properties are improved [11, 12], as well as the resistance to fatigue phenomena [11, 13] and corrosion-related mechanical failures [11, 12, 14]. Thanks to the fact that Cr is retained in solid solution, the corrosion resistance in many environments can be preserved or even increased, as in chloride (Cl^-)-containing solutions [9, 11, 15–17]. The biocompatibility is usually maintained [11, 18, 19], so that the surface treated alloys can be considered for biomedical applications. Moreover, the formation of a supersaturated phase affects wettability [11, 20–22], and electric [11, 17] and magnetic [11, 23, 24] properties.

However, the formation of expanded austenite is not a peculiarity of low-temperature treated austenitic stainless steels, but it can also be obtained in other fcc alloys, as nickel (Ni) [25–27] and cobalt (Co) [25, 28, 29] alloys, and fcc medium- and high-entropy alloys [30, 31]. Although the studies on low-temperature treatments of austenitic stainless steels have flourished, it has not been the same for the other alloy types, and the full potential of this surface modification strategy has to be explored. Compared to other surface engineering processes, low-temperature thermochemical treatments give many advantages. The produced expanded phases are a modification of the parent matrix, and hence they are not subjected to detachment as coatings having insufficient adhesion. Compared to processes which modify only the passive film leaving the underlying metal unchanged, the obtained hardened surface layers allow for a significant enhancement in the resistance to wear and fatigue phenomena. Thanks to the low treatment temperatures, the risk of distortion of the components is reduced and the energy consumption of the process is decreased. The treatments can be carried out using gaseous [32, 33], plasma [34, 35], and salt bath [36, 37] processes or even using a solid precursor [38]. The control of interstitial atom feeding is simpler in the gaseous processes, even if the removal of the passive layer of the alloy for having a homogeneous treatment may require a pre-treatment of the component [32]. Plasma-based treatments can easily remove the passive layer, can be faster and more efficient than gaseous processes, and they have a reduced environmental impact [34]. Till date, gaseous, plasma, and salt bath low-temperature thermochemical treatments are commercially available [39, 40].

Despite the opportunities that are offered by low-temperature treatments for the surface modification of fcc alloys, the research has been mainly focused on austenitic stainless steels, as well as the reviews on this topic reported in international journals [11, 15, 25, 41–46] or as book chapters [7, 32, 34, 39, 40, 47–49]. In the reviews, the description of the modified layers has become more and more accurate as the research has progressed and the characteristics of the expanded austenite have been explored [7, 11, 25, 39–43, 45, 47, 48]. Different analysis techniques should be used for having a picture as complete as possible [45]. The surface engineering processes, which are suitable for low-temperature treatments, have been reviewed [7, 25, 32, 34, 40–43, 46–48], and the conditions for obtaining modified surface layers without Cr compounds have been indicated [7, 11, 25, 32, 39–41, 45–48], especially for AISI 300 series stainless steels, which are the focus of most of the studies and the reviews. Industrial applications have also been reported [25, 39–41]. The thermodynamics of the expanded austenite and the peculiar diffusion kinetics of interstitial atoms in the modified layer have been overviewed [7, 11, 25, 39, 44, 45], due to their scientific and technological importance, as well as the thermal stability of expanded austenite and its decomposition [7, 11, 25, 34, 39, 42]. The hardening effects and the hardness profiles are very important for technological applications, and they are relevant topics in all the reviews [11, 25, 32, 34, 39–42, 44–47], as well as the effects on the performance properties when wear and fatigue phenomena are a major concern [11, 25, 34, 40, 42, 47]. The relationship among the concentration of interstitial atoms, residual stress, and hardness profile has also been discussed [11, 25, 32, 39, 40, 44, 48], in view of the possibility of tailoring hardness profiles for specific applications. Another aspect of paramount importance regards corrosion behavior, which has been discussed in general reviews [11, 25, 34, 39–42] and dedicated overviews [15, 49]. Few reviews also consider the other properties which can be affected by low-temperature treatments, such as wetting behavior, biocompatibility, magnetic, and electric properties [11, 25].

Compared to austenitic stainless steels, less attention has been paid to the low-temperature treatments of other fcc alloys. The possibility of producing expanded austenite on Ni and Co alloys was briefly overviewed by Bell [41], and then more in depth by Dong [25] in 2010. Nitriding treatments were discussed for Ni alloys (in particular, Ni-Cr alloys), and carburizing treatments for Co-Cr alloys, highlighting the effects on hardness, wear, and corrosion resistance. In 2024, Calabokis et al. [27] reviewed the nitriding treatments of Ni-based Inconel 718, discussing hardness, wear, and corrosion properties. For medium- and high-entropy alloys, the studies on these treatments are at the very beginning, and Meijun et al. [50] only reported brief references to them when reviewing the treatments for improving friction and wear properties. As a matter of fact, a recent comprehensive review, which takes into account the studies on the low-temperature treatments of different types of fcc alloys is lacking.

The aim of the present review is to critically analyze and discuss the main studies regarding the low-temperature thermochemical treatments of fcc alloys, offering a picture as complete as possible. The characteristics of expanded austenite and the modified layers in which it forms are considered, and the effects of the treatments on different properties (hardness, tribological properties, corrosion behavior, wettability, biocompatibility, magnetic properties) are discussed. The influence of chemical composition of the alloys is analyzed taking into account different Fe, Ni and Co fcc alloys, and entropy alloys. Although austenitic stainless steels have already been extensively covered in many reviews, they are also overviewed here for facilitating the comparison with the other alloys and allowing a thorough discussion. The opportunities and challenges of these treatments are highlighted, and possible future directions for the investigation are suggested.

2 | Characteristics of Expanded Austenite

N and/or C surface alloying performed at low temperatures produces a supersaturated solid solution in fcc-based alloys. In austenitic stainless steels this phase is indicated as expanded austenite [33], or S-phase [41, 51], although in Ni alloys it is indicated as M phase [52]. For Fe, Ni, and Co alloys, the terms γ_N (N-rich) and γ_C (C-rich) are often used, and they are employed hereafter together with the popular "expanded austenite."

In the fcc lattice, interstitial atoms are usually accommodated in the larger octahedral sites (Figure 1a). As reported in Table 1, the maximum content of N and C in expanded austenite is well beyond the maximum solubility in fcc Fe, Ni, and Co in equilibrium conditions. The N content can also be larger than that detected in stable and metastable nitrides, usually having an fcc or hexagonal close-packed (hcp) lattice of metal atoms. It has to be noted that the fcc arrangement of metal atoms is maintained in the M_4N-type nitride, that is, the stable γ'-Fe_4N and the metastable Ni_4N (I-type) and Co_4N, in which the octahedral site at center of the lattice is occupied by a N atom (Figure 1b), and in the MN (M = metal atom) nitride, that is, the metastable FeN [69], NiN [70], CoN [71], the stable CrN [72], and the MN nitride formed in high-entropy alloys [73].

The solubilization of interstitial atoms beyond solubility limit, indicated as "colossal" supersaturation [8], causes an expansion

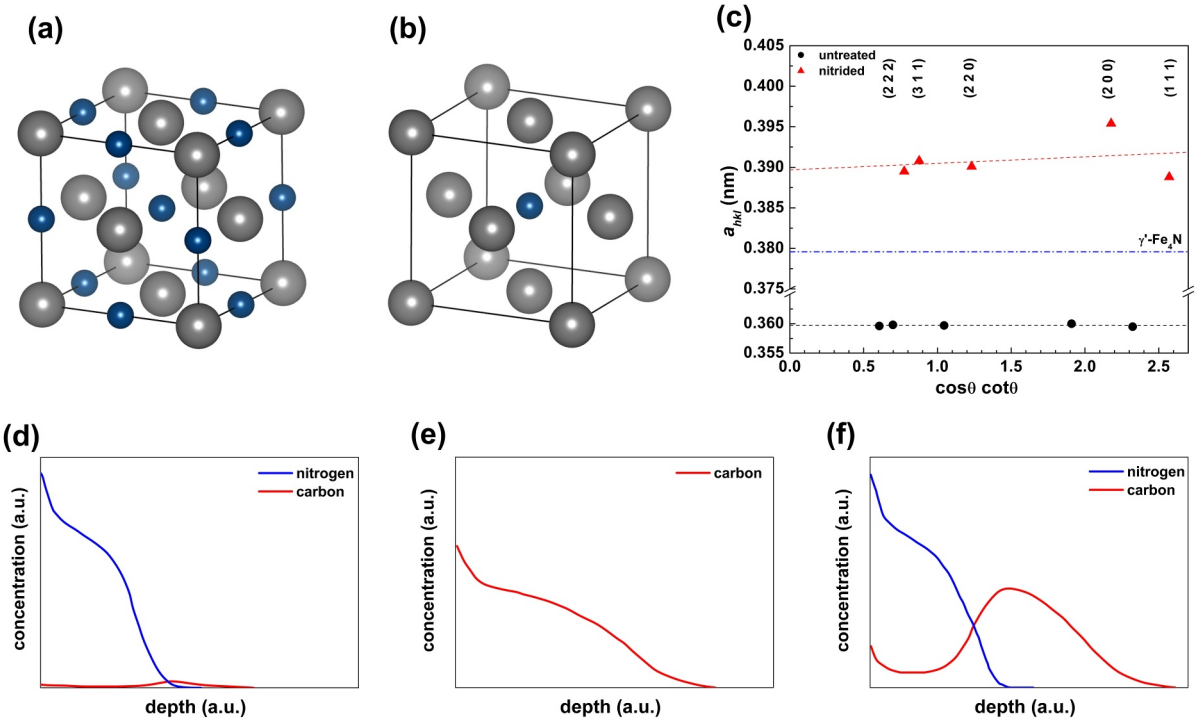

FIGURE 1 | Sketch of the fcc lattice (gray spheres) with the octahedral interstitial sites (blue spheres) (a), and of the M_4N-type nitride (M: gray spheres; N: blue sphere) (b); plot of lattice parameters a_{hkl} versus cosθ cotθ for AISI 316L untreated and plasma nitrided (data from ref. [53]) (c); qualitative trends of N and C concentration profiles in nitrided (d), carburized (e) and nitrocarburized (f) austenitic stainless steels.

TABLE 1 | N and C content in expanded austenite obtained in different fcc alloys and in stable/metastable phases. Regarding the space group, the lattice type of metal atoms is indicated in parentheses.

Phase	Space group	*N* (at.%)	C (at.%)	Reference
Expanded austenite (ASS) (max.)	$Fm\bar{3}m$ (fcc)	38	19	N: [54]; C: [55]
Expanded austenite (Ni alloys) (max.)	$Fm\bar{3}m$ (fcc)	31	18	N: [26, 56]; C: [57]
Expanded austenite (Co alloys) (max.)	$Fm\bar{3}m$ (fcc)	38	25	N: [58]; C: [59]
Expanded austenite (entropy alloys) (max.)	$Fm\bar{3}m$ (fcc)	43	13	N: [60]; C: [61]
γ-Fe (max.)	$Fm\bar{3}m$ (fcc)	10.3	9.23	N: [62]; C: [63]
γ'-Fe_4N	$Pm\bar{3}m$ (fcc)	19.3–20	—	N: [62]
ε-$Fe_{2-3}N$	$P6_322$ (hcp)	15–33	—	N: [62]
Ni (max.)	$Fm\bar{3}m$ (fcc)	~1	2.7	N: [64]; C: [65]
Ni_4N	$Pm\bar{3}m$ (I) (fcc) $I4/mmm$ (II) (fct)	20	—	N: [64]
Ni_3N	$P6_322$ (hcp)	25	—	N: [64]
ε-Co (max.)	$P6_3/mmc$ (hcp)	0	0	N: [66]; C: [67]
α-Co (max.)	$Fm\bar{3}m$ (fcc)	5	4.1	N: [68]; C: [67]
Co_4N	$Pm\bar{3}m$ (fcc)	20	—	N: [66]
Co_3N	$P6_322$ (hcp)	25	—	N: [66]

Abbreviation: ASS, austenitic stainless steels.

of the fcc lattice. This expansion can be particularly large in N-rich expanded austenite, thanks to the larger effective atomic radius and the possible higher concentration of N atoms than those of C. In the fcc lattice, N can reach up to a 0.61 occupancy of octahedral interstitial sites (i.e., the number of interstitial atoms per metal atom in a fcc lattice) in austenitic stainless steels [74]. It is unclear whether, with a further content increase, all the N atoms are hosted in the octahedral sites, leading to a tendency toward the ordered structure of NaCl-type nitride γ'''-FeN, or if they also tend to occupy the tetrahedral sites, typical of the ZnS-type nitride γ''-FeN [10, 69].

The presence of expanded austenite can be easily inferred with x-ray diffraction (XRD) analysis. The peaks of this phase are shifted toward lower angles, if compared to those of the fcc lattice of the parent phase. This shifting was the reason for the name "S-phase," given by Ichii et al. [51] to the phase formed in low-temperature nitrided 18–8 austenitic stainless steel. Expanded austenite has a XRD pattern with peculiar features, when it forms on a substrate which constrains its expansion. The peaks are usually broadened, and, when a fcc lattice is assumed as an indexing base, the lattice parameter calculated from the *d*-spacing of the (200) plane is always larger than that calculated from (111), (220), (311) or (222) planes [11, 25, 31, 43, 53, 75–77] (Figure 1c). This anisotropic expansion is not observed when thin homogeneous foils of expanded austenite are analyzed [54, 78], or thinned and unconstrained samples are studied with transmission electron microscopy (TEM) technique using the selected area electron diffraction (SAED) analysis [31, 75, 76]. Therefore, it can be hypothesized that the anomalous peak-shift of expanded austenite is due more to the characteristics of the modified layer as a whole, than to a peculiar behavior of this phase. It has been suggested that the peak shift is related to the anisotropy of the elastic modulus of the fcc lattice [43], in particular when it is subjected to an elasto-plastic transition [79], the presence of extended stacking faults [53], and compressive residual stresses changing with depth [80]. It has to be supposed that a combination of all these factors can contribute to the peak shape and position.

Another peculiarity is the N and C concentration profile observed in the expanded austenite layer. The N and C profiles cannot usually be fitted with the complementary error function, describing a concentration-independent diffusion. An enhanced diffusion is registered for both N and C when low-temperature treatments are carried out on austenitic stainless steels, and it has been supposed that this behavior depends on interstitials concentration [81, 82], the occurrence of residual stresses in the forming modified layer [81–83], and the "trapping effect," which is exerted by Cr atoms especially on N atoms [82, 83]. When nitriding is carried out, a high N concentration is detected at the surface, then there is a steep decrease to a lower content forming a more or less extended plateau, followed by a steep decrease [12, 19, 26, 43, 60, 74, 77, 82] (Figure 1d). In the carburized specimens, the high C content at the surface is followed by a gradual decrease [8, 12, 17, 19, 43, 57, 84, 85] (Figure 1e). When both N and C alloying is performed, in a single nitrocarburizing treatment or in sequential nitriding/carburizing treatments, an outer N-rich expanded austenite region and an inner C-rich expanded austenite layer form [19, 43, 86–89] (Figure 1f). As a consequence, a smoother interstitials profile is obtained, as compared to that of nitrided specimens [43].

Interstitials solubilization causes a solid-solution strengthening effect, so that an increased yield strength is expected for expanded austenite if compared to the matrix. However, the lattice expansion is so huge that the related strain cannot be

accommodated only elastically, and local plastic deformations occur [11]. Slip bands are usually observable at the surface and in the cross-section, and rotation and swelling of the grains are also registered [53, 75]. Depending on the stacking fault energy (SFE) of the alloy, extended stacking faults can also be produced, which are related to the formation of the so-called N-induced hcp ε'-martensite, ε_N'. It is not clear whether ε_N' can be considered strictly a martensite phase, which forms from γ_N through an fcc-to-hcp martensitic transformation [75], or it is simply the result of a cluster of stacking faults [90]. The chemical-induced strains, which are ascribable to the interstitials content and change with depth, and thermal strains, due to a gradient in thermal shrinking during cooling, produce a complicated state of stress in the modified layer, with high compressive residual stresses (up to a few GPa) at the surface [8, 13, 44]. The residual stress as a function of depth can be changed modifying the composition profile of solubilized interstitial atoms [91].

Solid solution strengthening, strain hardening due to local plastic deformations and residual compressive stresses contribute to an enhanced hardness increase [8], which has beneficial effects for both tribological properties and fatigue resistance. The hardness profiles usually resemble the concentration profiles of the interstitial atoms. In nitrided samples, high hardness values are detected at the topmost region, forming a more or less wide plateau, and then there is a steep decrease to matrix values [53, 86, 91, 92]. In carburized specimens, a gradual decrease in the hardness values is observed [8, 13, 84–86]. In nitrocarburized samples, high values are detected at the surface, forming a plateau, and then there is a gradual decrease to matrix values [86, 88, 93].

Expanded austenite can also exert a beneficial effect in corrosive environments [9, 15, 25], as it can also be inferred by the excellent resistance of the modified layer to chemical etching. In Cr-containing alloys, Cr remains in solid solution in the fcc lattice, and hence it promotes the formation of a protective passive film. In austenitic stainless steels, it was observed that N and/or C surface alloying causes an entrapment of the interstitial atoms in the passive film [94, 95]. The presence of these interstitials is particularly effective in Cl^--containing environments, such as NaCl solutions, sea water, biological fluids, and a significant increase in corrosion resistance is observed. In austenitic stainless steels, the presence of N within the passive film tends to enhance its stability, protective effect, and the bonding at oxide-metal interface [96]. N atoms form preferential bonds with Cr and Fe, and therefore the active dissolution of these metal atoms is hindered [97]. When the passive film is broken and localized corrosion phenomena begin, N atoms are released from the oxide layer and the underlying N-rich expanded austenite, and they may react with H^+ forming NH_4^+, causing a local alkalization of the acidic environment present in pit or crevice [96–98]. The presence of C within the passive layer and solubilized in expanded austenite may have similar beneficial effects, even if the occurring phenomena are not completely clear [9]. It may be hypothesized that C addition is able to hinder passive film dissolution [99, 100], as well as metal dissolution, thanks to fairly strong metal-C bonds [101]. Moreover, when C atoms are released, HCO_3^- may form and an increase in pH within the pit or crevice can occur, so that the conditions for the formation of a stable passive layer can be restored [9]. When the environment causes general corrosion, such as in H_2SO_4 aqueous solutions, different behaviors are reported. The corrosion resistance of modified layers consisting of N-rich expanded austenite can be comparable to that of the untreated alloy only when other phases (ε_N' and/or nitrides) do not form, otherwise a worsening of corrosion resistance is observed [12, 102]. Conversely, C-rich expanded austenite tends to reduce the susceptibility to corrosion [12, 17, 103].

As a non-equilibrium phase, expanded austenite tends to transform when the service temperature is too high. The transformation rate and its mechanism depend on the alloy composition [11, 104, 105]. However, the incubation time for the formation of compounds is usually estimated as thousands of hours at ~300°C [104–107], and longer for lower service temperatures.

3 | Austenitic Stainless Steels

Austenitic stainless steels are CrNi (AISI 300 series), CrMn (AISI 200 series), and Ni-free Fe-based alloys, which maintain the austenite fcc structure thanks to a balance between ferrite forming elements (in particular, Cr) and austenite forming elements (Ni, manganese [Mn], N, C). Their excellent corrosion resistance in many environments, due to the formation of a self-healing passive film, allows for their use in a wide variety of applications, from components for the power engineering and chemical industries to body implants, kitchenware, and furniture [108]. However, their low hardness and poor tribological properties are a limitation for extending their use further on. Low-temperature thermochemical treatments have proven to be the suitable processes for enhancing surface hardness while maintaining or even improving corrosion resistance thanks to the formation of expanded-austenite modified surface layers. The low-temperature treatments have been applied to many austenitic stainless steels, as reported in Table 2. The indicated references are only a small part of the studies devoted to this steel type. An extended analysis of the characteristics and properties of low-temperature treated austenitic stainless steels and references to more studies are reported in reviews on this topic, such as [7, 9–11, 15, 25, 39–49].

The formation of N- and/or C-rich expanded austenite causes local plastic deformations that are well observable at the surface [10, 16, 17, 20–22, 53, 75, 109, 126] (Figure 2a), producing a roughness increase [16, 20, 21], and in the cross-section [10, 16, 53, 75, 109, 112] (Figure 2b). The slip lines are more numerous in Mn-rich alloys [16, 21, 75, 109] and when a high N content in γ_N is attained [16, 75]. The formation of ε_N' [10, 16, 20, 21, 75, 112, 126] (Figure 2c) is promoted by N and alloy elements, as Mn, which decrease SFE [16, 20, 21, 75, 109, 112, 127].

The modified layer is continuous, fairly homogeneous, and highly resistant to chemical etching. In the nitrided specimens, a single layer [12, 19, 33, 75] or two-sublayers [10, 16, 21, 112, 118, 126] (Figure 2b) are observable, while only one layer is detectable in carburized samples [12, 13, 17, 19, 33]. In nitrocarburized alloys two sub-layers are present, an outer N-rich γ_N

TABLE 2 | Austenitic stainless steel types subjected to low-temperature thermochemical treatments.

Alloy type	Composition (wt.%)	Treatment type	References
AISI 304	C: 0.08; Cr: 18–20; Ni: 8.0–10.5	Triode-plasma nitriding (*T*: 450°C; *t*: 4, 20 h)	[75]
		Triode-plasma nitriding (*T*: 400, 450°C; *t*: 20 h)	[109]
		Plasma nitriding (*T*: 400°C; *t*: 8 h)	[110]
		Plasma nitrocarburizing (*T*: 375–475°C; *t*: 2 h)	[111]
AISI 304L	C: 0.03; Cr: 18–20; Ni: 8–12	Glow-discharge plasma nitriding (*T*: 400, 430°C; *t*: 5 h)	[112]
		Plasma source ion nitriding (*T*: 400°C; 4 h)	[94, 96]
		Hollow cathode plasma source carburizing (*T*: 450°C; 4 h)	[100]
		Gaseous carburizing (unspecified)	[17]
		Plasma nitrocarburizing (*T*: 400°C; *t*: 3–10 h)	[113]
AISI 316	C: 0.08; Cr: 16–18; Ni: 10–14; Mo: 2–3	Gaseous nitriding (*T*: 445°C; *t*: 22 h)	[33]
		Gaseous nitriding (*T*: 420°C; *t*: 13 h)	[23]
		Plasma nitriding (*T*: 450–550°C; *t*: 5 h)	[114]
		Plasma nitriding (*T*: 450°C; *t*: 12 h)	[115]
		Plasma nitriding (*T*: 430°C; *t*: 15 h)	[116]
		Gaseous carburizing (unspecified)	[17]
		Gaseous carburizing (*T*: 500, 507°C; *t*: 4, 6 h)	[33]
		Gaseous carburizing (*T*: 450°C; *t*: 20 h)	[101]
		Plasma carburizing (*T*: 450; *t*: 12 h)	[115]
		Plasma carburizing (*T*: 500°C; *t*: 15 h)	[116]
		Plasma nitrocarburizing (*T*: 450–500°C; *t*: 12 h)	[115]
		Plasma nitrocarburizing (*T*: 430°C; *t*: 15 h)	[116]
AISI 316L	C: 0.03; Cr: 16–18; Ni: 10–14; Mo: 2–3	Gaseous nitriding (*T*: 430, 450°C; *t*: 18, 20 h)	[33]
		Plasma assisted nitriding (*T*: 400°C; *t*: 15 min–8 h)	[22]
		Plasma assisted nitriding (*T*: 420°C; *t*: 1–4 h)	[117]
		Glow-discharge plasma nitriding (*T*: 380, 400°C; *t*: 5 h)	[20]
		Glow-discharge plasma nitriding (*T*: 400, 430°C; *t*: 5 h)	[112]
		Glow-discharge plasma nitriding (*T*: 430°C; *t*: 0–5 h)	[118]
		Glow-discharge plasma nitriding (*T*: 430°C; *t*: 5 h)	[53, 119]
		Glow-discharge plasma nitriding (*T*: 360, 380°C; 3 h)	[16]
		Glow-discharge plasma nitriding (*T*: 400°C, *t*: 5 h)	[18]
		Glow-discharge plasma nitriding (*T*: 400–500°C; *t*: 5 h)	[120]
		Plasma nitriding (*T*: 415°C; 15 h)	[12]
		Plasma nitriding (*T*: 380–420°C; *t*: 2 h)	[121]
		Triode plasma nitriding (*T*: 450°C; *t*: 5 h)	[122]
		Active screen plasma nitriding (*T*: 440°C; *t*: 6 h)	[123]
		Plasma nitriding (*T*: 450°C; *t*: 4 h)	[124]
		Gaseous carburizing (*T*: 510°C; *t*: 4 h)	[33]
		Gaseous carburizing (*T*: 450°C; *t*: Unspecified)	[95]
		Gaseous carburizing (unspecified)	[8, 24]
		Gaseous carburizing (*T*: 470°C; *t*: 30 h)	[13]
		Plasma carburizing (*T*: 470°C; *t*: 15 h)	[12, 99, 103]
		Triode plasma carburizing (*T*: 475°C; *t*: 3 h)	[122]
		Active screen plasma nitrocarburizing (*T*: 430°C; *t*: 4 h)	[89]

(Continues)

TABLE 2 | (Continued)

Alloy type	Composition (wt.%)	Treatment type	References
		Active screen plasma nitrocarburizing (T: 440°C; t: 6 h)	[123]
		Triode plasma nitrocarburizing (combined carburizing + nitriding)	[122]
AISI 316Ti	C: ≤ 0.08; Cr: 16.5–18.5; Ni: 10.5–13.5; Mo: 2.0–2.5; Ti: 5 × C ≤ 0.70	Low energy ion implantation (LEII) nitriding (T: 350–500°C; t: 1.5–3 h)	[125]
		Plasma immersion ion implantation (PIII) nitriding (T: 450, 500°C; t: 1, 1.5 h)	[105]
ASTM F138 (316LVM)	C: ≤ 0.03; Cr: 17–19; Ni: 13–15; Mo: 2.25–3.00	Plasma nitriding (T: 430°C; t: 15 h)	[19, 116]
		Plasma carburizing (T: 500°C; t: 15 h)	[19, 116]
		Plasma nitrocarburizing (T: 430°C; 15 h)	[19, 116]
AISI 321	C: 0.08; Cr: 17–19; Ni: 9–12; Ti: 5 × C ≤ 0.70	Plasma source ion nitriding (T: 380°C; 4 h)	[97, 98]
		Plasma source ion nitriding (T: 280, 380°C; t: 4, 6 h)	[102]
AISI 202	C: 0.065; Cr: 17; Ni: 4.1; Mn: 7.7; N: 0.15	Glow-discharge plasma nitriding (T: 400°C; t: 5 h)	[20]
		Glow-discharge plasma nitriding (T: 400, 430°C; t: 5 h)	[112]
		Glow-discharge plasma nitriding (T: 360, 380°C; 3 h)	[16]
		Glow-discharge plasma nitriding (T: 330, 380°C; 8 min, 5 h)	[21]
ASTM F1586	C: ≤ 0.08; Cr: 19.5–22.0; Ni: 9–11; Mn: 2.00–4.25; Mo: 2.0–3.0; N: 0.25–0.50	Plasma nitriding (T: 430°C; t: 15 h)	[19, 116]
		Plasma carburizing (T: 500°C; t: 15 h)	[19, 116]
		Plasma nitrocarburizing (T: 430°C; 15 h)	[19, 116]
AISI 904L	C: ≤ 0.02; Cr: 19–21; Ni: 24–26, Mo: 4–5; Cu: 1.2–2.0	LEII nitriding (T: 350–500°C; t: 1.5–3 h)	[125]
		PIII nitriding (T: 450°C; t: 1 h)	[105]
		Gaseous carburizing (unspecified)	[17, 24]
Fe-19Cr-35Ni-1.2Si	C: 0.05; Cr: 18.5; Ni: 34.9; Si: 1.2	Triode-plasma nitriding (T: 400–450°C; t: 4, 20 h)	[75]
		Triode-plasma nitriding (T: 400, 450°C; t: 20 h)	[109]
Fe-20Cr-24Ni-6Mo	C: 0.02; Cr: 20.41; Ni: 24.34; Mo: 6.14; N. 0.10	Gaseous carburizing (unspecified)	[24]
Fe-0.2C-17Cr-11Mn-3Mo-0.5N	C: 0.2; Cr: 17.7; Ni: 0.05; Mn: 10.5; Mo: 3; N: 0.53	Glow-discharge plasma nitriding (T: 360, 380°C; t: 3 h)	[16]
		Glow-discharge plasma nitriding (T: 360–400°C; t: 1–5 h)	[126]
Fe-17Cr-20Mn-0.5N	C: 0.03; Cr: 17.4; Ni: 0.8; Mn: 18.9; N: 0.5	Triode-plasma nitriding (T: 400–450°C; t: 4, 20 h)	[75]
		Triode-plasma nitriding (T: 400, 450°C; t: 20 h)	[109]

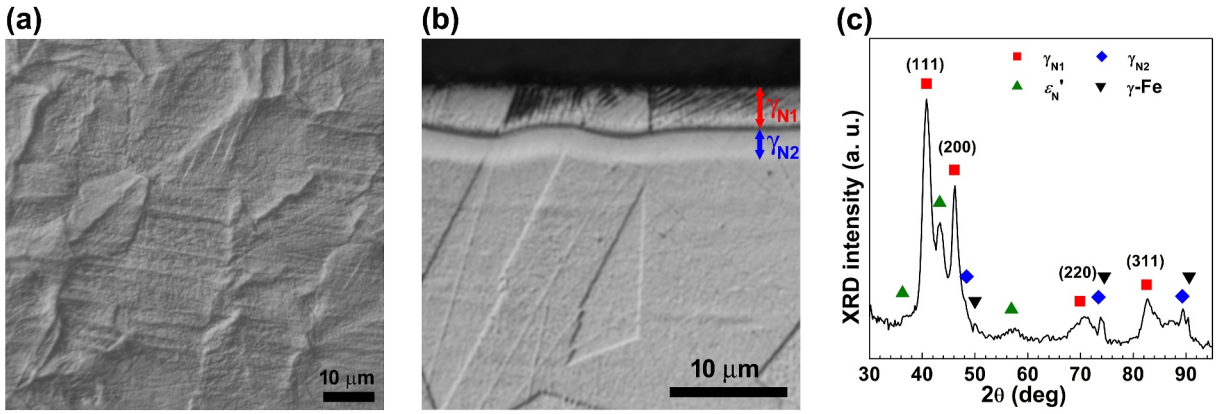

FIGURE 2 | Surface morphology (a), cross-section micrograph (b) and XRD pattern of nitrided (380°C) AISI 202 (c) (adapted from ref. [10] under the terms of CC-BY license. Copyright 2022 by the author).

layer and an inner C-rich γ_C layer [19, 89, 111]. The reason for the formation of two apparent distinct sub-layers in nitrided samples is not clear. In XRD patterns, two γ_N phases are detected, one with higher N content and larger lattice expansion present in the outer part, and another, with lower interstitial content and a smaller expansion, formed in the inner part [10, 16, 21, 112, 126] (Figure 2c). Different hypotheses were suggested, including the effect of N concentration profile [81], local high residual stresses [128], and the formation of a C-rich inner expanded austenite layer, due to C segregation [117]. As a matter of fact, the formation of a layered structure of two γ_N phases having different lattice expansions was observed in both AISI 316Ti and AISI 904L, and it seemed to depend on treatment conditions [125].

Many analyses were carried out in order to elucidate whether the expanded austenite is indeed a supersaturated solid solution. A preferential bonding between Cr and N atoms was registered [129], and Cr-N regions having a short-range order (SRO) were detected [130]. Moreover, long-range ordered (LRO) regions having a γ'-Fe_4N-order (γ_N') are observed in the topmost part of the modified layer, where the N concentration is larger and exceeding that typical of the γ'-Fe_4N nitride [127]. In the inner part of the modified layer, this order tends to be lost, and only SRO Cr-N regions are present in a disordered γ_N matrix [127]. The formation of γ_N', as well as of ε_N', was also detected in nitrocarburized alloys [113].

The formation of Fe-based nitrides, γ'-Fe_4N and ε-$Fe_{2-3}N$, may be promoted by γ_N' and ε_N', and they tend to form as precipitates especially along the slip lines or at grain boundaries [53, 112, 120, 126, 127]. The formation of Cr compounds is usually observed when treatment temperature exceeds 450°C for nitriding [105, 120, 131], and 550°C for carburizing [131]. However, the formation of Cr and Fe compounds depends not only on the treatment conditions (temperature, duration, interstitial atoms supply), but also on the steel composition [75, 112, 126]. As an example, the nitriding temperature for producing a nitride-free γ_N layer tends to decrease as the Mn content in the alloy increases and the Ni content is lower [75, 112, 126].

In the topmost part of the modified layer a maximum N concentration up to ~38 at.% was registered [54]. However, solubilized N also depends on alloy composition. As an example, nitriding at 400°C for 20 h produced modified layers having a N concentration at the surface of 26.9 at.% in AISI 304 (Fe-18Cr-8Ni), 34 at.% in Fe-17Cr-20Mn-0.5N steel and 24 at.% in Fe-19Cr-35Ni-1.2Si [75, 109], so that a role of Mn in promoting a supersaturated solid solution can be supposed. A maximum C content up to 19 at.% was detected in the carburized samples [55]. The thickness of the modified layer usually ranges from a few microns to a few tens of microns, depending on the treatment conditions (type, temperature, and duration) and alloy composition. As an example, using the same treatment conditions, thicker modified layers were observed as the Mn content increases and Ni decreases [16], or the Ni content increases [124].

The service temperature of expanded austenite is limited by its decomposition and the formation of Cr compounds. For γ_N, the incubation time for the formation of CrN is thousands of hours at ~300–350°C [105, 106], and for γ_C, the formation of carbides requires thousands of hours at 350°C [107].

All the low-temperature treatment types allow for an enhancing of surface hardness. The hardness profile is similar to the interstitial atoms concentration profile (Figure 3a). In nitrided samples, the profile maintains the step-like trend [53, 86, 112, 115, 119]. A maximum hardness value of ~14.2 GPa was measured in nitrided AISI 316L [118], and in Fe-17Cr-20Mn-0.5N steel, having a large amount of ε_N', a value as high as ~17.7 GPa was registered [109]. In carburized specimens, values as high as ~10.7 GPa [86] were measured at the surface, followed by a smooth decrease [8, 86, 115]. The nitrocarburizing treatment produces higher values at the surface than those obtained with carburizing, and a more gradual decrease than that observed in nitrided specimens [86, 115].

The enhancement in surface hardness promotes an increase in tribological properties [8, 109] (Figure 3b) and fatigue resistance [8], the latter even at high temperatures (300–500°C) [13]. The adhesive wear, typical of the untreated austenitic stainless steels, becomes an oxidative-mild wear for treated steels, and wear resistance is enhanced as the hardness and thickness of the modified layer increase. The high surface hardness attained in nitrided specimens allows for reducing wear loss in different test configurations in dry conditions [12, 109, 110, 114, 115, 122, 131]. However, the high N content and the concurrent large residual stress together with the step-like hardness profile may limit the load-bearing capacity of the modified layer [109, 115, 122], and a brittle behavior may occur [109]. When large amounts of ε_N' form together with γ_N, as in the Mn-rich Fe-17Cr-20Mn-0.5N steel, no evident brittle behavior was observed, suggesting a positive role of ε_N' in counteracting the embrittlement effect of N supersaturation [109] (Figure 3b). Wear resistance in a corrosive environment depends not only on wear conditions, but also on the environment itself, which can restore the protective passive film or cause an active material dissolution [12, 114]. Thanks to the smooth hardness profile, carburized steels usually have an enhanced load-bearing capacity and wear resistance in different test configurations [8, 12, 115, 122, 132], even in corrosive-wear conditions [12]. An improved wear resistance was usually observed for nitrocarburized specimens, thanks to the favorable combination of high hardness values at the surface, given by the outer γ_N layer, and the smooth hardness profile, given by the inner γ_C layer, which enhances the load-bearing capacity of the modified layer [89, 115, 122].

Corrosion resistance can be preserved or even increased thanks to the formation of expanded austenite. As summarized in refs. [9, 15], the success or failure of the modified surface layer depends on the microstructure and phase composition of the layer itself in the specific environment. An excellent corrosion resistance was observed for the modified layers consisting mainly of γ_N in the presence of Cl^-, such as aerated and deaerated NaCl solutions [16, 21, 53, 109, 120, 123, 126], mixed saline solutions such as those simulating body fluids [18, 116, 119], when pitting [16, 109, 123, 126] or crevice [120] corrosion phenomena are considered. Electrochemical Impedance Spectroscopy (EIS) analysis highlights an increased polarization resistance of the

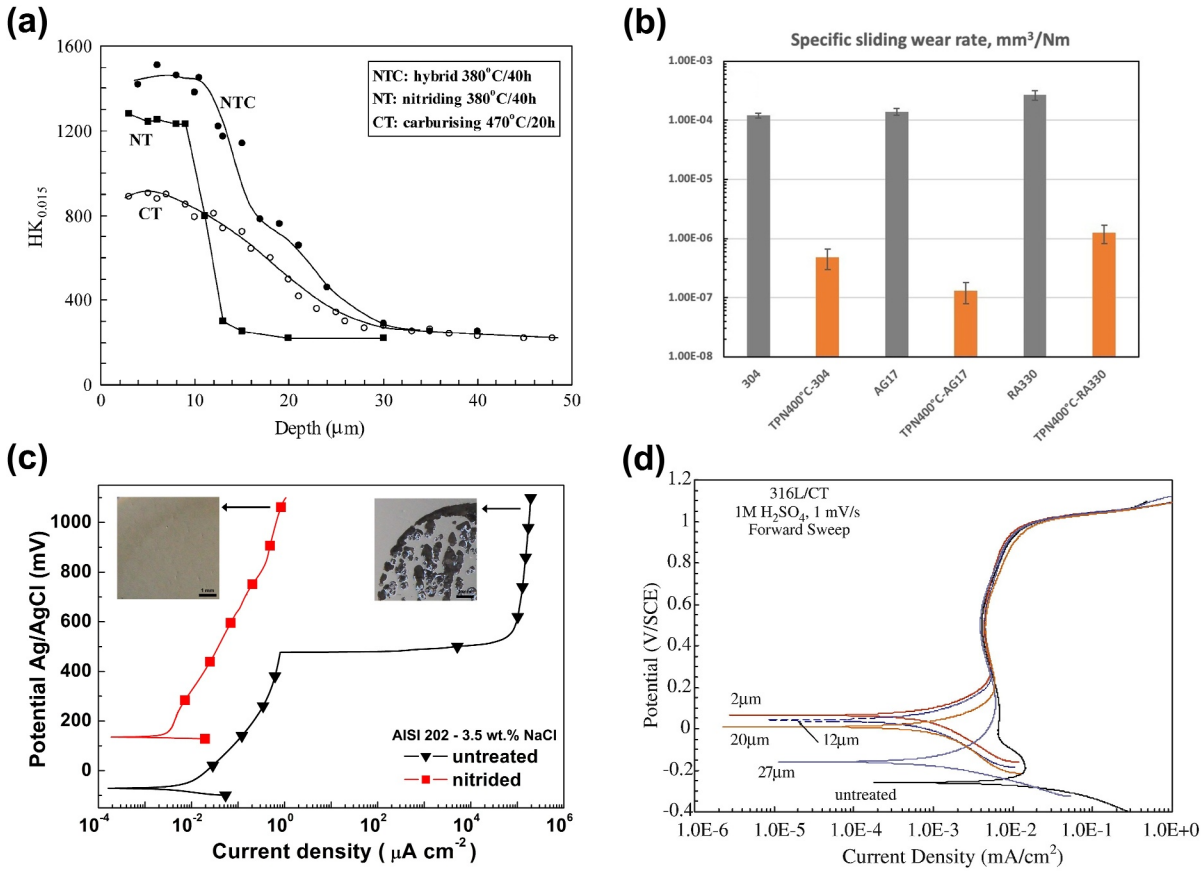

FIGURE 3 | Microhardness profiles of nitrided (NT), carburized (CT) and nitrocarburized (NTC) CrNi austenitic stainless steel (reprinted from ref. [86], copyright 2005, with permission from Elsevier) (a); specific sliding wear rate of untreated and nitrided (400°C) AISI 304 (304), Fe-17Cr-20Mn-0.5N (AG17) and Fe-19Cr-35Ni-1.2Si (RA330) (dry ball-on-plate reciprocating configuration, WC-Co ball) (reprinted from ref. [109], copyright 2021, with permission from Elsevier) (b); potentiodynamic polarization curves of untreated and nitrided (380°C) AISI 202 (solution: 3.5 wt.% NaCl) (adapted from ref. [10] under the terms of CC-BY license. Copyright 2022 by the author) (c); potentiodynamic polarization curves of untreated and carburized (470°C) (different depth in the modified layer) AISI 316L (solution: 1M H_2SO_4) (reprinted from ref. [103], copyright 2010, with permission from Elsevier) (d).

nitrided specimens [16, 18, 21, 126]. The potentiodynamic polarization curves usually show higher corrosion potential and pitting potential values and lower anodic current density in the passive branch, if compared to those of the untreated steel [10, 16, 18, 21, 109, 112, 119, 126] (Figure 3c). The improvement in corrosion resistance to pitting phenomena for a plasma nitrided AISI 321 tested in a 3 wt.% NaCl solution was observed in the pH range 4–11 [98]. However, the ability of a γ_N layer to repassivate depends on the damage extent, and repassivation is possible when the depth of the crevice or pits is not too large [16]. The effect of alloy elements was studied, particularly taking into account the synergy between molybdenum (Mo) and N in enhancing corrosion resistance [16, 112, 126]. The concurrent formation of ε_N' or small amounts of nitrides together with γ_N does not adversely affect the corrosion resistance [16, 21, 102, 109, 112, 126], as well as a fairly rough surface (2D finishing, Ra ~ 0.2 μm) [21, 112]. On the contrary, when a large amount of nitride precipitates forms, the corrosion resistance significantly decreases [102, 109, 120, 126]. The beneficial effect of the γ_N layer depends on its characteristics, and in particular its thickness, N content and the presence of nitride precipitates. Therefore, treatment conditions (temperature, duration, and N supply) should be carefully chosen for obtaining a N-rich, nitride-free and thick γ_N layer. Carburizing treatments allow for an improved corrosion resistance as long as the carbon soot formed during the treatment and the topmost layer rich in carbide precipitates are carefully removed [99, 116], otherwise the presence of carbides precipitates at the surface can cause a worsening of corrosion resistance [99, 101]. An enhancement in corrosion resistance was also registered for nitrocarburized steels [89, 116, 123]. A slower pit formation was observed for nitrocarburized AISI 316L specimens, if compared to nitrided samples, suggesting a synergy of N and C atoms in hindering corrosion phenomena [123]. When Cl^--free solutions are considered, a different picture was observed. The formation of a heterogeneous microstructure consisting of γ_N with ε_N' and/or nitrides promotes corrosion phenomena in H_2SO_4, however for a layer consisting of γ_N alone the corrosion resistance is preserved [102]. A good corrosion resistance was also registered for carburized steels in which a carbide-free C-rich γ_C layer was produced [17, 103] (Figure 3d).

The change in surface microstructure and roughness produced by low-temperature thermochemical treatments also causes a change in wettability characteristics. The wetting behavior depends on the properties of the surface (topography, chemical

composition, eventual surface contamination), as well as the liquid type and drop size. For nitrided specimens, a moderate hydrophilic (apparent contact angle [CA] < 90°) [19–22, 121] or hydrophobic (CA > 90°) [20–22, 121] behavior was observed with a decrease or increase in CA if compared to that of the untreated alloy. These different behaviors may be ascribed to the effect of surface roughness [20–22], and the presence of polar groups at the surface [121]. In the presence of liquids of low surface tension (ethanol and rapeseed oil), very low CA values were detected, and hence an oleophilic behavior may be supposed [21]. A decrease in CA was also observed for nitrocarburized specimens [19], when compared to that of the untreated steel, while an increase was registered when carburizing treatment was applied, with CA values almost reaching 90° [19].

The enhancement in corrosion resistance has suggested that low-temperature thermochemical treatments can also be applied to body implants. The biocompatibility of surface treated steels has been assessed *in vitro* using different cellular lines, such as osteoblast [19], endothelial cells [18, 119], human blood mononuclear cells [18], cultured on nitrided [18, 19, 119], nitrocarburized [19], and carburized [19] specimens. The possibility of using duplex treatments, such as a nitriding treatment followed by oxidation [119] or collagen coating [18], was also explored. Good levels of cytocompatibility were usually observed for the surface treated specimens [18, 19, 119]. Regarding hemocompatibility and thrombogenicity properties, lower platelet adhesion and activation were registered for nitrided specimens when the treatment produced a smooth, more hydrophilic surface [121].

The formation of expanded austenite also changes the magnetic properties of the surface layers. Austenitic stainless steels have a paramagnetic behavior at room temperature. When N is solubilized, γ_N remains paramagnetic as long as the N content is lower than ~14 at.%, and the lattice expansion is smaller than 4.2%–5% [133]. With higher N concentration γ_N becomes a soft ferromagnet [23, 133]. It was hypothesized that this ferromagnetism is related to Cr-N preferential bonding, which causes a removal of Cr 3*d* electrons from the valence band [133]. When N content reaches a value in the range 27.5–35.5 at.%, γ_N becomes again paramagnetic [23]. It is interesting to note that for these concentrations the presence of LRO γ'-like nitride was detected [23], but γ_N as a whole had not the ferromagnetic behavior registered for γ'-Fe_4N. The importance of lattice expansion, and a possible role of alloy elements, was highlighted by Schuler et al. [24] in carburized AISI 316L, AISI 904L and Fe-20Cr-24Ni-6Mo. Due to the larger C solubilization (18.5–19 at.%), which produced a larger lattice expansion (3.8–3.9%) of γ_C, AISI 904L and Fe-20Cr-24Ni-6Mo had ferromagnetic regions in the modified layer, while for AISI 316L γ_C, which had a 13 at.% maximum C content and a smaller lattice expansion (~2.5%), remained paramagnetic.

4 | Austenitic Steels

Even if Cr has usually a key role in the formation of expanded austenite, low-Cr and Cr-free austenitic steels are also able to form this supersaturated phase. N-rich expanded austenite was observed when low-temperature nitriding treatments were performed on Invar Fe-Ni alloy [128, 134], high-Mn twinning-induced plasticity (TWIP) austenitic steels [135, 136], and hot-stamping die SDHA steel [137] (Table 3).

In austenitic steels, the formation of expanded austenite is competitive with that of γ'-Fe_4N nitride, and it can be confused with this phase in XRD diffraction patterns. Modified layers consisting of a thin γ'-nitride layer on the top of an expanded austenite layer were observable on Invar 36 [134]. A similar microstructure was observed on Cr-free 24Mn-2Al-0.45C TWIP steel, but the XRD pattern ascribable to the nitride appeared widened, suggesting a variable N content [135]. As a matter of fact, the N profile smoothly decreased from ~40 at.%, [135], a concentration significantly higher than that of γ'-Fe_4N [62], and a similar smooth trend was observed for the microhardness profile [135]. Microscopy analysis of the cross-section showed that the modified layer has a two-layer structure, probably due more to a C-enrichment in the inner part of the layer than to a difference in phase composition. However, both the layers appear as a modification of the austenite matrix [135]. It may be hypothesized that a transition from a disordered N-rich fcc lattice toward an ordered γ' lattice occurred as the N content increased. The presence of Cr in the steel seems to promote the formation of expanded austenite, which enhances surface hardness [137] and corrosion resistance in NaCl solution [136].

5 | Ni-Based Alloy

Ni-based alloys have a very good combination of mechanical, chemical, and physical properties, which make them suitable

TABLE 3 | Austenitic steel types subjected to low-temperature thermochemical treatments.

Alloy type	Composition (wt.%)	Treatment type	References
Invar	Ni: 34	Ion beam processing nitriding (*T*: 400°C; *t*: 15 min)	[128]
Invar 36	Ni: 36	Triode plasma nitriding (*T*: 400–450°C; *t*: 4, 20 h)	[134]
24Mn-2Al-0.45C (TWIP)	C: 0.45; Mn: 24; Al: 2	Active-screen plasma nitriding (*T*: 350–480°C; *t*: 10 h)	[135]
25Mn-3Cr-3Al-0.3C-0.01N (TWIP)	C: 0.3; Mn: 25; Al: 3; Cr: 3; N: 0.01	Gaseous nitriding (*T*: 400–600°C; *t*: 2 h)	[136]
SDHA steel	C: 0.63; Mn: 10.25; Cr: 3.22; Mo: 1.78; V: 1.92	Plasma nitriding (*T*: 560°C; 4 h)	[137]

for many industrial applications, especially when corrosion and/or heat resistance is the main concern [138, 139]. Low-temperature thermochemical treatments have been applied to many Ni-based alloys, as summarized in Table 4. Most of the studies are focused on nitriding of precipitation-hardenable Inconel 718 [27], which is used in high-temperature aerospace applications, corrosion-resistant components in oil and gas extraction, and in nuclear engineering.

When low-temperature nitriding is performed on pure Ni, a significant N solubilization does not usually occur and expanded austenite is not detected [76, 128, 140]. Ni nitrides, which might be formed at low temperatures [153–155], are present in very low amounts [128] or they are even undetectable [76, 140]. On the contrary, modified surface layers, consisting of the supersaturated solid solution of N and/or C in the Ni fcc lattice γ, formerly indicated as M phase [52], can be observed in many Ni alloys, and they are usually similar to those observed in low-temperature treated austenitic stainless steels. However, their characteristics, such as layer microstructure and phase composition, thickness, and hardness, depend on both alloy elements and treatment conditions.

After low-temperature nitriding, the typical features observed for austenitic stainless steels are also detected for many Ni alloys. On the surface, the typical swelling of the grains, due to plastic deformation, is observable [26, 76], and hence an increase in the surface roughness is registered [92, 148]. The modified layer is usually well resistant to chemical etching, and a single layer [92, 141, 142, 144, 146, 148, 150], two sublayers [141, 142, 144, 149], and even three distinct layers [147] were observed, depending on the alloy type and treatment conditions. As an example, in Ni-Ti alloys, gaseous nitriding at 400°C for durations in the range 18–65 h produced a single γ_N layer on Ni-2Ti but two sublayers with two distinct γ_N phases with different lattice expansions on Ni-4Ti [142]. On the contrary, plasma nitriding at 600°C for 3 h produced a single γ_N layer on Ni-7Ti alloy [141]. Two sublayers were observed in Ni-Ti [142], Ni-Cr [141], Ni-V [141], Nichrome [144], Inconel 625 [145], Inconel 690 [56, 147], Inconel 718 [76], while three sublayers were detected in Inconel 690 [147]. It may be hypothesized that the formation of sublayers, as well as of two or even three γ_N with different lattice parameters, is related to the trend of N content profile in the nitrided layer and therefore of depth-dependent residual stresses. In fact, a high N content and compressive stress values (up to a few GPa) are present in the regions near the surface, while significantly lower N content and residual stress values are registered in the bottom part of the modified layer [56, 142].

In binary Ni alloys, nitriding is able to produce γ_N when selected alloy elements are present [52, 141]. Expanded austenite is observed when Ni is alloyed with titanium (Ti), Cr, niobium (Nb), vanadium (V), and Mn, but not when alloying is done with aluminum (Al), silicon (Si), zirconium (Zr), hafnium (Hf), tantalum (Ta) and Mo [52, 141]. In Ni-copper (Cu) Monel, no significant hardening effect due to nitriding is observed [156]. In Ni-Fe Permalloy, very small XRD peaks of expanded austenite were detected [128]. It has to be noted that, using the same treatment conditions, the expansion of the Ni lattice, as observed by using XRD, and the thickness of the nitrided layer depend significantly on the alloy element type. As an example, by nitriding at 450°C, the shift of expanded austenite peaks was larger for Ni-7Ti alloy as compared to that of Ni-30Cr [141]. When nitriding was performed at 400°C, 3 h, the surface microhardness of Ni-30Mn (~2 GPa) was slightly higher than that of the untreated alloy, while for Ni-10Nb and Ni-30Cr was ~4.6 GPa, and for Ni-7Ti increased up to ~7.4 GPa [141]. A similar trend was observed for the thickness of the nitrided layer, with the Ni-30Mn alloy having the thinnest layer, while Ni-7Ti had the thickest one. Moreover, the thickness of the nitrided layer increased as the alloy content was higher [141, 142].

Modified surface layers consisting of expanded austenite are also observed on Ni-based superalloys. Depending on the alloy elements and thermomechanical treatments, the microstructure of these alloys may consist of either nearly 100 vol.% of fcc phase, γ, or γ with intermetallic precipitates (up ~70 vol.% [26, 152]), usually obtained with an aging treatment for optimizing mechanical properties, especially at high temperatures. Due to the fairly high temperature of the aging treatment (620–845°C [157]), N and/or C surface alloying must be performed as a final step and thus, it involves not only the Ni matrix but also the precipitates. Depending on superalloy composition and thermomechanical treatments, the precipitates may have different shape, sizes (from few tens of nanometers to few micrometers), and may be coherent, semi-coherent or not coherent with the matrix. The main precipitate is γ'-Ni_3Al (Al partially substituted by Ti, Nb), having an ordered fcc structure ($L1_2$). Depending on the γ/γ' misfit, the shape of the precipitate and its coherency with the matrix change: high misfit promotes a cubic shape and high coherency, while a lower misfit promotes the formation of spheroidal precipitates partially coherent with the matrix [152]. γ''-Ni_3Nb (Nb, partially substituted by Ti) has an ordered body-centered tetragonal structure ($D0_{22}$) and forms (semi-)coherent disc-shaped precipitates. Incoherent precipitates of the stable δ-Ni_3Nb, having an ordered orthorhombic structure ($D0_a$), can form from γ'' at temperature higher than 850°C [158]. The alloy content is different in the matrix and precipitates. As an example, in aged conditions, the γ matrix of Inconel 718 is rich in Cr (> 20 at.%), while the γ' and γ'' precipitates have a very low Cr content (~< 3 at.%), but they have a significant amount of other nitride forming elements (γ': > 5 at.% Al and Ti; γ'': > 16 at.% Nb) [158]. As observed above, Ni-Al alloys are not able to form expanded austenite layers, although Ni-Nb and Ni-Ti alloys can [141], and this fact has repercussions for the N solubilization in γ' and γ'' precipitates. When the alloy consists of nearly 100% γ phase, such as Haynes 230Li [26] or Inconel 690 [56], the modified surface layer is analogous to that observed in austenitic stainless steels, with the typical step-like N profile, having the characteristic plateau with a fairly high (~25 at.%) N content. Similar microstructure and N profile shape are also observed in polycrystalline alloys having a significant amount of intermetallic precipitates, such as Inconel 718, which has γ' and γ'' of few tens of nanometer (typically 25 vol.% as a whole) [26, 76], or Udimet 720Li, having a multimodal γ' distribution (typically 40–45 vol.%) [26, 152] (Figure 4a). The comparable maximum N contents and N profiles of Haynes 230Li, Inconel 718 and Udimet 720Li, treated with the same nitriding parameters (400°C, 1, 4 h), suggested that intermetallic precipitates had a N content similar to that of the surrounding γ matrix [26].

TABLE 4 | Ni-based alloy types subjected to low-temperature thermochemical treatments.

Alloy type	Composition (wt.%)	Treatment type	References
Ni	Ni > 99.99	Ion beam processing nitriding (*T*: 400°C; *t*: 15 min)	[128]
	Ni: 99.95	Low-energy high-flux implantation nitriding (*T*: 450, 475°C; *t*: 1 h)	[140]
	Ni > 99.2	Triode plasma nitriding (*T*: 450°C; *t*: 20 h)	[76]
Ni-Ti	Ti: 1, 1.5, 4, 7	Dc glow-discharge nitriding (*T*: 400–800°C; *t*: 1–9 h)	[52, 141]
	Ti: 2, 4	Gaseous nitriding (*T*: 400°C; *t*: Up to 70 h)	[142]
Ni-Cr	Cr: 5, 10, 15, 20, 30	Dc glow-discharge nitriding (*T*: 400–800°C; *t*: 1–9 h)	[52, 141]
Ni-Nb	Nb: 1, 4, 10	Dc glow-discharge nitriding (*T*: 400–800°C; *t*: 1–9 h)	[52, 141]
Ni-V	V:1, 5, 10, 15	Dc glow-discharge nitriding (*T*: 400–800°C; *t*: 1–9 h)	[52, 141]
Ni-Mn	Mn: 10, 30	Dc glow-discharge nitriding (*T*: 400–800°C; *t*: 1–9 h)	[52, 141]
Permalloy	Fe: 19.2	Ion beam processing nitriding (*T*: 400°C; *t*: 15 min)	[128]
Nichrome	Cr: 20.98; Si:1.26	LEII nitriding (*T*: 350–500°C; *t*: Up to 1.5 h)	[104, 143]
	Cr: 20; Si: 1.5	Low-energy high-flux implantation nitriding (*T*: 450, 475°C; *t*: 1 h)	[140]
	Cr: 21.1; Si: 1.5; Fe: 1.5	Gaseous nitriding (*T*: 400, 440°C; *t*: 20 h)	[144]
Nimonic 80, 90, 95, 100	Cr: 12.1, 20; Co: 0, 16–20; Mo: 0, 6.2; Al: 1.4–4.6; Ti: 1.2–3.3	Gaseous nitriding (*T*: 400, 440°C; *t*: 20 h)	[144]
Inconel 625	Cr: 25; Fe: 5; Mo: 5; (Nb + Ta): 2	Ion beam processing nitriding (*T*: 400°C; *t*: 15 min)	[128]
		Plasma nitriding (*T*: 420°C; *t*: 20 h)	[145]
		Plasma nitriding (*T*: 430, 500°C; *t*: 15 h)	[146]
Inconel 690	Cr: 29.25; Fe: 10.35; Al: 0.14; Ti: 0.24	Pulsed dc discharge nitriding (*T*: 300–400°C; *t*: 15 min–6 h)	[147]
		Pulsed dc discharge nitriding (*T*: 400°C; *t*: 0.5–36 h)	[56]
Inconel 718	Cr: 18.9; Fe: 19.3; Nb: 5.4; Mo; 3.5 Al: 0.6; Ti: 1.0	Triode plasma nitriding (*T*: 400–450°C, 700°C; *t*: 4, 20 h)	[76]
		R.f. plasma nitriding (*T*: 400°C, *t*: 1, 4 h)	[26]
		Active screen plasma nitriding (*T*: 400°C; *t*: 20 h)	[148]
		Hot wall plasma nitriding (*T*: 400–500°C; *t*: 6 h)	[92]
		Pulsed plasma nitriding (*T*: 400, 450°C; *t*: 4 h)	[149]
		Salt bath nitriding (*T*: 425–500°C; *t*: 4–16 h)	[150]
		Gaseous carburizing (*T*: 510–570°C; *t*: 28 h)	[151]
		Gaseous carburizing (510°C; *t*: 28 h)	[57]
Haynes 230	Cr: 26.5; Fe: 3.4; Mo: 1.3; W: 4.8; Co: 5.3; Al: 0.7; Ti: 0.1	R.f. plasma nitriding (*T*: 400°C, *t*: 1, 4 h)	[26]
Udimet 720Li	Cr: 17.3; Mo: 1.8; W: 0.5; Co: 14.1; Al: 5.2; Ti: 5.9	R.f. plasma nitriding (*T*: 400°C, *t*: 1–16 h)	[26, 152]
MC2	Cr: 9.3; Mo: 1.3; W: 2.6; Co: 5.1; Al: 11.2; Ti: 2.5; Ta: 2.0	R.f. plasma nitriding (*T*: 400°C, *t*: 1–16 h)	[26, 152]
MarM200-DS	Cr: 10.2; W: 4.0; Co: 9.6; Al: 9.9; Ti: 2.4; Nb: 0.7	R.f. plasma nitriding (*T*: 400°C, *t*: 4–16 h)	[152]
René N4	Cr: 10.3; Mo: 1.2; W: 1.9; Co: 8.1; Al: 8.3; Ti: 5.2; Ta: 1.3; Nb: 0.3	R.f. plasma nitriding (*T*: 400°C, *t*: 4–16 h)	[152]

A comparable swelling effect of the grains at the surface was also observed, and therefore a similar elasto-plastic behavior was hypothesized [26]. Further studies on Inconel 718 suggested that N incorporation is reduced in γ', while γ'' has a N-induced lattice expansion comparable to that of the surrounding γ_N [76], but the N distribution is fairly uniform in the modified layer [149] (Figure 4b). In monocrystalline alloys, as MC2, which has ~70 vol.% of coherent cuboidal γ' (Al: 14.8 at.%; Ti: 3.1 at.%) precipitates (~400 nm size), the N content in the plateau is significantly reduced (~10–12 at.%) [26, 152] (Figure 4a). It was assessed that, using the same nitriding conditions, the thickness of the modified layer was smaller than that obtained in super-alloys as Haynes 230Li or Inconel 718 [26]. The analysis of N distribution showed that N was fairly uniform in the γ matrix

and γ' precipitates only within a ~200-nm depth, while in the inner part of the modified layer low-N γ' precipitates were present in a channel-like γ_N [26, 152] (Figure 4c). A thicker (~2 μm) N-rich layer in both γ' and γ matrix was observed in the single crystal alloy René N4, having cuboidal γ' precipitates with a higher Ti content (Al: 8 at.%; Ti: 6–7 at.%) [152]. An intermediate behavior was observed in directionally solidified MarM200-DS alloy, having large cuboidal coherent γ' precipitates with a lower Ti content (Al: 14.8 at.%; Ti: 3.7 at.%). In this alloy, the precipitates were N-rich within the first 500 nm from the surface, while in the inner part of the nitrided layer N was present only in the surrounding γ matrix [152]. It was also observed that cracks might occur in the part of the layer where γ_N and N-rich γ' were present [152]. The comparison of the nitriding behavior of polycrystalline and single crystal alloys suggested that the main parameter which influences γ' nitriding is its composition, that is, the Al substitution by elements as Ti and Nb [152]. N uptake is lower as the γ' composition is closer to Ni_3Al. A thicker N-rich homogeneous ($\gamma' + \gamma$) nitrided layer is obtained as the content of Al-substitutes, such as Ti, is larger. Moreover, taking into account that the formation of γ_N may induce local plastic deformations, the propagation of dislocation in the precipitates, which is related to their composition-dependent shear strength, may also promote γ' nitriding. On the contrary, size, orientation or coherency of γ' precipitates seem not to influence their nitriding behavior. It has to be noted that the nitriding front remains almost flat, regardless of the alloy composition, and no lateral or backside N incorporation in cuboidal γ' precipitates was observed. It was hypothesized that a specific, high nitriding potential, related to a N-rich γ_N, is needed for allowing γ' nitriding. The main role of Al in hindering the nitriding of γ' precipitates was also recently assessed using first-principles calculations [159]. It was observed that, even if the interaction between Al and N is stronger than that between Ni and N, N prefers to occupy the larger octahedral interstitial site surrounded by six Ni atoms, than the smaller one surrounded by both Ni and Al atoms, due to the larger atomic radius of Al than that of Ni. Moreover, the $(002)_{\gamma/\gamma'}$ coherent plane tends to act as a two-dimensional barrier, hindering the migration of N atoms from γ to γ'. Further studies, based on first-principles calculations, confirmed that the partial substitution of Al with Ti promotes nitriding of γ' decreasing the energy barrier of N penetration [160]. Nitriding is also facilitated by doping with Ta, while tungsten (W) has a weak effect on N penetration [160].

Nitride formation depends on both treatment parameters (temperature, duration, N feeding), as well as alloy composition. Ni_4N was detected together with γ_N in a Nichrome alloy, subjected to Low-Energy Ion Implantation (LEII) nitriding at 350 and 375°C for 30 min [143]. When the treatment was performed at 400°C, the XRD peaks ascribable to nitride disappeared, and only the peaks belonging to γ_N and a low amount of CrN were observable. Alloy element nitrides, such as CrN, AlN, TiN, may form at temperatures as low as 400°C [26, 144, 149]. As treatment temperature or duration increases, alloy elements nitrides, in particular CrN, are detected [76, 92, 144–146, 150], and they are observable as precipitates inside the expanded austenite matrix [76, 144, 146, 150], or forming a more or less continuous layer [76, 144]. The formation of large amounts of CrN causes the decomposition of expanded austenite, and therefore a low-N γ is detected [76, 149, 150].

Different maximum N contents were registered in the different alloys. A N content up to ~6.8 at.% was measured in a Ni-4Ti alloy, nitrided at 400°C for 65 h without the formation of precipitates or clusters [142]. In nitrided (400°C, 90 min) Ni-20Cr Nichrome, a N content of ~17 at.% was detected [143]. In superalloys, such as Inconel 690, Haynes 230Li, Inconel 718, Udimet 720Li, MC2, and René N4, the N content detected at the nitrided (400°C) surface was ~27–31 at.% [26, 56, 152]. The thickness of the modified layers is usually some micrometers, and it depends on both treatment conditions and alloy element composition. As expected, due to diffusion phenomena, the nitrided layer becomes thicker as the treatment temperature and/or time increase [26, 76, 92]. However, at fairly high temperatures, such as 700°C [76], the thickness is usually smaller than that produced at temperatures lower than about 450°C, due to the formation of a large amount of alloy element (in particular, Cr) nitrides. It may be supposed that nitrides hinder the N diffusion and solubilization in the Cr-depleted Ni-rich matrix. Alloy element composition also influences modified layer thickness. As an example, when Haynes 230Li, Inconel 718 and Udimet 720Li were plasma nitrided at 400°C for 4 h, they had a ~6-μm thick nitrided layer, which was thicker than that produced on AISI 316L stainless steel (~4 μm) [26]. On the contrary, Nichrome had a thinner nitrided layer, if compared to AISI 316Ti, when LEII nitriding was performed at 400°C for 80 min [104].

The formation of a C-rich expanded austenite is also possible by means of low-temperature treatment. The studies on this topic are few and they are focused on Inconel 718 [57, 151]. When carburizing was carried out in the range 510–570°C, the modified layer was homogeneous and almost featureless, and it was unetched by chemical etchant in both the solution-annealed [57] and aged [151] alloy conditions. A maximum C content of ~18 at.% was registered [57, 151]. The modified layer has a thickness of several microns, depending on previous heat treatment and carburizing parameters. As an example, carburizing the solution-annealed alloy at 510°C for 28 h produced a modified layer ~20-μm thick [57], while using the same treatment conditions the modified layer is ~12-μm thick for the aged alloy [151].

Low temperature thermochemical treatments can significantly increase the surface hardness. The surface hardness value depends on the interstitial content and thickness of the modified layer, the formation of alloy element nitrides and/or carbides, and the presence of intermetallic precipitates, which may also solubilize N and/or C. As an example, when Inconel 718 was plasma nitrided at 400°C for 20 h, the modified layer, consisting mainly of γ_N with more or less N-rich Ni-Al precipitates, had a surface hardness of ~15.3 GPa [76]. When the treatment temperature was increased at 450°C and CrN nitrides precipitates formed, a surface hardness of ~16.4 GPa was detected [76]. The formation of a thick modified layer having a significant amount of nitrides increased the surface hardness further on, and values as high as ~26 GPa (600°C, 4 h) were reached [161]. The microhardness profile is similar to the N profile, with very high

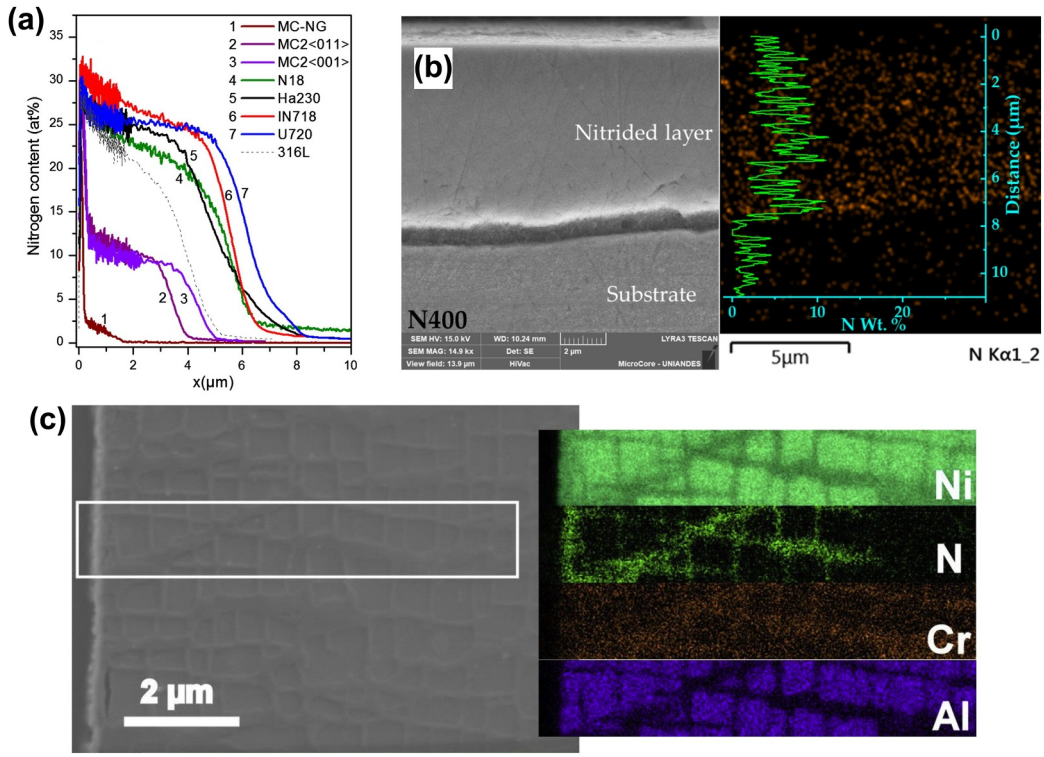

FIGURE 4 | N concentration profiles of different nitrided (400°C) Ni alloys (reprinted from ref. [26], copyright 2013, with permission from Elsevier) (a); cross-section microstructure and EDS maps of nitrided (400°C) Inconel 718 (reproduced from ref. [149] under the terms of CC-BY license. Copyright 2023 by the authors) (b), and nitrided (400°C) MC2 alloy (adapted from ref. [152], copyright 2019, with permission from Elsevier) (c).

values near the surface followed by a fairly steep decrease to matrix values [92, 145], with a trend similar to that observed for low-temperature nitrided austenitic stainless steels [11, 25]. Low-temperature carburizing produces hardened layers reaching a surface hardness as high as ~15 GPa [57]. Hardness profiles are similar to the C profile, that is, a maximum hardness value at the surface and then a smooth decrease to matrix values [57, 151].

The effects of hardened layers on tribological properties have been studied mainly on Inconel 718. In dry conditions, a threefold reduction of the wear rate was registered for γ_N layers tested in pin-on-disk configuration [92]. A γ_N layer with a low amount of nitrides is also able to improve scratch resistance [145, 149], and it also decreases the volume loss in micro-abrasion wear tests [145]. The formation of a fairly large amount of nitrides, as observed at high temperature, can increase the wear resistance further on [92, 161]. The role of the tribosystem as a whole was highlighted by corrosion-wear studies, performed in reciprocating sliding configuration in a 0.6 M NaCl solution [148]. The γ_N layer reduced the wear rate by an order of magnitude when AISI 52100 steel balls were used as counterparts, while no significant effect was observed using Si_3N_4 balls, due to the occurrence of (micro-)abrasion wear phenomena. In erosion-corrosion tests, carried out in a 3.5 wt.% NaCl + 5 vol.% H_2SO_4 + 100 g/L Al_2O_3 particles, the γ_N layer could reduce mass loss [150]. The highest corrosion resistance (nitriding 475°C, 4 h) was observed when CrN precipitates did not form, and the modified layer thickness was sufficient to provide a hardened layer, while avoiding too thick layers which cracked under very high compressive residual stresses.

A beneficial effect is exerted by expanded austenite when corrosion resistance is taken into account. The maintenance or even the increase in corrosion resistance in NaCl solutions is observed for nitrided alloys when nitrided layers consist of γ_N only [92, 148], or having a small amount of compound precipitates [76]. In EIS analysis, Nyquist plots of low-temperature nitrided samples had larger semicircles than those of the untreated alloys, suggesting a higher resistance to general corrosion phenomena [92]. In potentiodynamic tests, a shift of the corrosion potential toward nobler values was registered for nitrided alloys as compared to that of the untreated alloys [76, 92, 148] (Figure 5a), and higher open circuit potential (OCP) values were detected [148]. However, a significant difference in the pitting potential and current density in the passive branch were not usually observed when low-temperature nitrided and untreated samples were compared [76, 149]. The formation of a low amount of (CrN) nitrides did not significantly impair corrosion resistance [76, 149]. On the contrary, when a fairly high amount of nitrides formed, using treatment temperatures higher than about 450°C, corrosion resistance worsened [76, 92]. An increase in crevice corrosion resistance was observed when a low amount of CrN was present together with γ_N (Figure 5b), while for layers consisting of CrN + low-N γ a significant damage was registered [149]. γ_C improves corrosion

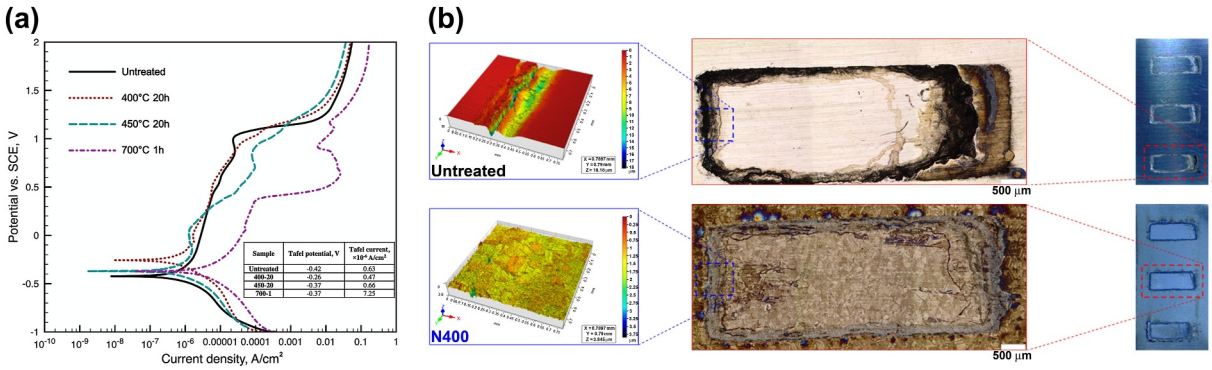

FIGURE 5 | Potentiodynamic polarization curves of untreated and nitrided Inconel 718 (solution: 3.5 wt.%) (reproduced from ref. [76], copyright 2022, with permission from Elsevier) (a); surface morphology after crevice tests for untreated and nitrided (400°C) (N400) Inconel 718 (solution: 3.56 wt.% NaCl) (adapted from ref. [149] under the terms of CC-BY license. Copyright 2023 by the authors) (b).

resistance in NaCl solutions. Higher corrosion potential values were observed for carburized (510°C, 28 h) Inconel 718 in both solution-annealed and aged conditions when it was tested in 0.6 M NaCl solution [151]. An improvement in crevice corrosion resistance was also registered [151].

Thermal stability of expanded austenite was assessed using both dedicated tests or evaluating the microstructure stability during the treatment. γ_N is stable at 400°C for durations up to about a few hours, while it tends to decompose into nitrides for longer durations [56, 104]. In the temperature range 200–300°C, thousands of hours were hypothesized for the incubation time of its decomposition [104]. Regarding γ_C, a 24-h long exposure at 350°C, simulating the core working temperature of a boiling water reactor (BWR), did not cause significant change in the characteristics of the surface layer [57]. On the contrary, tests carried out at 800°C, 1 h, in air and in vacuum, for simulating "emergency" conditions of a BWR, showed that γ_C suffered a loss of C due to outward and inward C diffusion, and Cr carbide precipitates formed. A softening of the hardened layer in a ~5-µm thick surface zone occurred. A similar behavior was observed when carburized specimens were irradiated with 1.5 MeV protons, which caused the precipitation of nano-sized Cr carbides [57].

Magnetic properties of N and/or C expanded austenite formed in Ni alloys have not been explored. Ni is ferromagnetic, while its nitrides or carbides are paramagnetic or ferromagnetic depending on composition [162, 163]. A magnetic behavior was observed for a N-rich Inconel 690 coating obtained with magnetron sputtering at 400°C, which might be ascribable to the formation of a MN-type fcc-based nitride together with a N-containing γ [56, 164].

6 | Co-Based Alloy

Co-based alloys are employed in many applications, ranging from components for the aerospace industry to orthopedic implants. The main alloy element is Cr, and the further addition of C and other alloy elements (Mo, Ni, W, etc.) allows for obtaining wear-resistant, heat-resistant, and/or corrosion resistant grades. Thanks to the very good corrosion resistance and good biocompatibility, some Co-Cr-Mo and Co-Cr-Ni grades are used in biomedical applications. Low-temperature treatments have been applied to Co alloys, in particular to high-C wear-resistant grades and Co-Cr-Mo corrosion-resistant grades, as summarized in Table 5.

Co has a hcp structure, ε-Co, which becomes fcc, α-Co, at 422°C. By adding alloy elements, the fcc structure can be retained at low temperatures, and therefore the alloys are usually a mixture of the two structures, with a large amount of retained fcc. Interstitial N and C are strong stabilizers of the fcc lattice, so that a transformation of hcp into fcc lattice may occur when N and/or C surface alloying is carried out.

The typical features of the modified layer are observed in the low-temperature treated specimens, as slip lines at the surface [29, 173] and in the cross-section [28, 84, 165, 166, 171], and a high resistance to chemical etching [84, 165, 170, 172].

The effect of N addition in Co-Cr alloys consisting mainly of hcp ε-Co was studied by Akhlaghi et al. [165] (Figure 6a). By nitriding at 400°C for 1 h, N was retained in solid solution and a N-rich expanded ε phase, ε_N, was obtained, having a maximum N content of ~20 at.%. As treatment duration or temperature increased, ε_N became unstable and it transformed gradually into γ_N. A 3-h nitriding at 450°C produced a modified layer consisting mainly of γ_N, reaching a maximum N content of ~22 at.% [165]. As treatment duration was longer, γ_N tended to decompose into Cr nitrides and low-N fcc and hcp phases, and the reversed fcc-to-hcp transformation was observed. Thicker layers were produced as treatment temperature and/or time increased; moreover, thicker layers were obtained in 10 at.% (~9 wt.%) Cr alloys, if compared to 15 at.% (~13.4 wt.%) Cr alloy.

A continuous modified layer, mainly consisting of γ_N, is also observable on Co-Cr-Mo [28, 29, 77, 172, 173] and Co-30Cr-19Fe [167] (Figure 6b). A two-layer microstructure is also observed [29, 173]. XRD analysis usually shows the characteristic peaks of expanded austenite [58, 77, 172, 175], but the presence of two γ_N having different lattice expansions is reported [104]. As treatment temperature, duration or N feeding increases, CrN precipitates are produced [58, 77, 167, 172, 173]. Cr nitrides can also be formed at low temperatures, depending on the alloy composition. As an example, in Co-30Cr-19Fe, nitrided at 350°C for 20 h, CrN was observed [167], while in Co-Cr-Ni-W-Fe

TABLE 5 | Co-based alloy types subjected to low-temperature thermochemical treatments.

Alloy type	Composition (wt.%)	Treatment type	References
Co-Cr	Cr: 9, 13.4	Gaseous nitriding (*T*: 400, 450°C; *t*: 1–24 h)	[165]
Stellite 21	Cr: 27; Mo: 5.5; Ni: 2.5; C: 0.3	Plasma carburizing (*T*: 400–500°C; *t*: 15 h)	[166]
		Plasma nitrocarburizing (*T*: 400–550°C; *t*: 10–20 h)	[87]
Co-30Cr-19Fe	Cr: 29.9; Fe: 19.1; Mo: 0.3; W: 0.2; C: 0.2	Plasma nitriding (*T*: 350, 400°C; 20 h)	[167]
		Plasma nitrocarburizing (*T*: 380°C; *t*: 3–15 h)	[168]
Co-28Cr-6Mo wrought (ASTM F1537—UNS R31537, ISO 5832-12 [Alloy 1])	Cr: 26–30; Mo: 5–7; C: ≤ 0.14	R.f. plasma nitriding (*T*: 400°C; *t*: 1–20 h)	[77]
		PIII nitriding (*T*: 300–550°C; *t*: 1 h)	[58]
		Plasma nitriding (*T*: 400°C; *t*: 4 h)	[29]
		Gaseous carburizing (Kolsterizing) (*T*: < 500°C; *t*: Unspecified)	[59, 84, 169]
Co-28Cr-6Mo wrought—(ASTM F1537—UNS R31538)	Cr: 26–30; Mo: 5–7; C: 0.15–0.35	Plasma nitriding (*T*: 325–400°C; *t*: 20 h)	[28]
		Plasma carburizing (*T*: 400–600°C; *t*: 10, 20 h)	[170]
		Plasma carburizing (*T*: 450°C; *t*: 10 h)	[171]
		Plasma nitrocarburizing (*T*: 325–375°C; *t*: 20 h)	[28]
		Gaseous nitrocarburizing (*T*: 527°C; *t*: 2 h)	[93]
Co-28Cr-6Mo cast—(ASTM F75)	Cr: 27–30; Mo: 5–7; C: ≤ 0.35	High power impulse magnetron sputtering plasma nitriding (*T*: 400°C; *t*: 4 h)	[172, 173]
HS188	Cr: 22; Ni: 22; W: 14; Fe: 3	Ion implantation (LEII and PIII) nitriding (*T*: 280–540°C; *t*: Up to 7 h)	[104, 174]
		PIII nitriding (*T*: 400°C; *t*: 2 h)	[175]

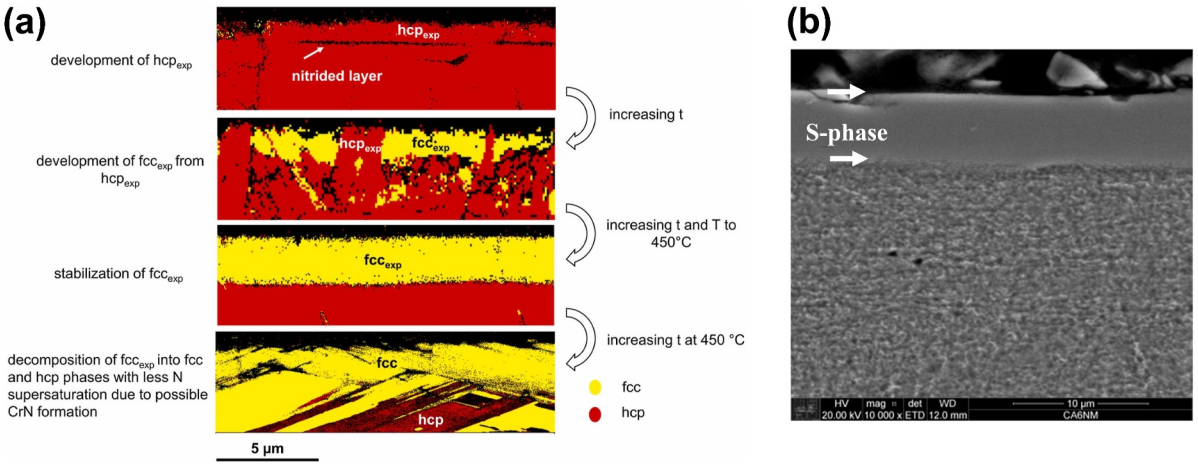

FIGURE 6 | Evolution of hcp and fcc phases in Co-15Cr alloy nitrided at 400 and 450°C (reproduced from ref. [165], copyright 2022, with permission from Elsevier) (a); cross-section microstructure of a nitrided (400°C) Co-30Cr-19Fe sample (reproduced from ref. [167], copyright 2019, with permission from Elsevier) (b).

HS188, nitrided at 420°C for 2 h, CrN was not detectable [174]. As the CrN content becomes larger, the decomposition of γ_N occurs [176].

A N content up to ~33 at.% was measured on Co-Cr-Ni-W-Fe HS188 alloy [175], and values as high as 34–38 at.% were registered on a Co-Cr-Mo ISO 5832-12 alloy [58]. The N concentration profile has usually a step-like trend [77, 165, 172]. The thickness of the N-rich layer is not significantly influenced by the Cr content of Cr-rich alloys. As an example, when L605 (Cr: 20 wt.%), HS188 (Cr: 22 wt.%) and Sy21 (Cr: 28 wt.%) alloys were nitrided at 340°C for 2 h, modified layers with comparable thickness were obtained [176]. The thickness of the modified layer increases as treatment temperature, duration or N feeding increases [104, 167, 172, 176]. By using the same treatment conditions (400°C, 1 or 2 h), the thickness of the modified layer

obtained on a HS188 Co-alloy was smaller than that obtained on an AISI 304 austenitic stainless steel [104, 175]. When large amounts of CrN formed, thinner modified layers were observed, if compared to CrN-free layers produced with the same treatment duration [176]. It was hypothesized that the CrN structure hinders an additional N uptake since the Cr-depleted Co matrix becomes unable to permit N transport.

In low-temperature carburized alloys, the formation of γ_C was observed in alloys consisting of both fcc and hcp phases, such as Stellite 21 [166], UNS R31537 [59, 84], and UNS R31538 [170]. On the top of the γ_C layer, a very thin (few tens of nanometers) carbide-rich topmost layer may be formed [170]. As the treatment temperature increases, carbides may precipitate [166, 170] and a lower C content in γ_C was detected [166]. A maximum C content of ~25 at.% was registered [59, 84]. The C profile, having a decreasing linear trend [84, 166], suggested that diffusion was influenced by internal stresses [84]. The modified layer thickness increases as the treatment temperature is higher [166].

When nitrocarburizing is performed, the modified layer consists of an outer N-rich zone, having a step-like trend of the N content, an inner C-rich zone, in which C content smoothly decreases [28, 87, 93, 168]. In plasma nitrocarburized Stellite 21, the thickness of the N-rich layer was smaller than that of the C-rich layer, irrespective of the treatment conditions [87]. A similar result was found for Co-30Cr-19Fe alloy [168]. Expanded austenite is observed to form from mixed fcc + hcp microstructures [87, 93, 168]. Alloy element nitrides may precipitate in the N-rich zone [93], as well as carbides may form [168]. CrN was detected when treatment temperature was 500°C or higher [87]. In Co-30Cr-19Fe alloy, the formation of nitrides and Fe_3C was observed using a treatment temperature as low as 350°C for durations of 9 h or longer [168]. As expected, the thickness of the modified layer increases as treatment temperature or time increases [28, 87, 168]. It has to be noted that the modified layer thickness of the nitrocarburized specimens tends to be higher than that of nitrided samples treated using the same temperature and duration. As an example, for 350-°C treated UNS R31538 the thickness of the modified layer is ~2.2 μm in nitrocarburized specimens, while only 1.5 μm in nitrided samples [28].

The formation of expanded austenite influences the surface microhardness. A maximum hardness value of ~12 GPa was measured in nitrided Co-10Cr alloy [165]. In Co-Cr-Mo alloys, a maximum hardness value of ~21.9 GPa was registered when the modified layer consisted mainly of γ_N, while when CrN precipitates also formed values as high as ~27 GPa were detected [172]. The microhardness profiles have the typical step-like trend [165]. The decomposition of γ_N and the formation of CrN with low-N fcc and hcp phases cause a decrease in the hardness values in the surface region [165]. When carburizing was carried out, a maximum hardness of ~15 GPa was measured [84], and the microhardness profile has a gradual decrease from the highest values at the surface to matrix values [171]. The formation of a nitrocarburized layer with nitride precipitates at the surface increases hardness up to 16 GPa [93].

The improvement in tribological properties is important for mechanical applications as well as for biomedical ones. The friction coefficient of a Co-Cr-Mo alloy, tested in unlubricated ball-on-disc conditions (load: 5 N; velocity: 0.1 m s^{-1}; counterpart: SUJ2 [AISI 52100] steel ball), was reduced from 0.8 for the untreated specimen to 0.4–0.5 for the plasma nitrided alloy [29]. In dry conditions, nitriding was effective in reducing wear loss [28, 172], especially when thick layers formed [28]. Debris due to the removal of thin γ_N layers or hard nitride precipitates may act as third-body abrasives, increasing wear loss [28]. The wear resistance was also improved in lubricated condition in Ringer's solution [28]. Nitrided ASTM F75 had an improvement in tribocorrosion resistance when tested in Hank's solution at anodic potential or in passivating conditions [177]. In cavitation-erosion conditions, as those obtained with a vibratory cavitation system, plasma nitriding of Co-30Cr-19Fe alloy allowed the increase in incubation time and a significant reduction in mass loss, especially when modified layers of adequate thickness and hardness were produced (400°C; 20 h) [167]. Corrosion-wear resistance is also enhanced by carburizing treatments, as highlighted by the studies on Stellite 21 tested in a 3.5 wt.% NaCl solution [166], and on Cr-28Cr-6Mo alloys tested in Ringer's solution [59, 171]. In particular, a significant reduction in wear loss was observed when testing was performed at potentials within the passive branch, that is, in conditions which promoted the passive layer reformation [59, 171]. When tests were carried out at OCP, or in cathodic conditions, in which the formation of the passive film was suppressed, the wear loss became comparable or even higher than that of the untreated samples, depending on the alloy type, characteristics of the modified layer and test conditions [59, 171]. The nitrocarburizing treatment is effective in improving wear resistance in dry conditions [28, 87, 93] and in presence of a potential corrosive environment such as NaCl solution [87] and Ringer's solution [28], especially when thick modified layers were produced. The increase in the resistance to cavitation-erosion phenomena, evaluated with a vibratory test, was observed for nitrocarburized Co-30Cr-19Fe [168]. The lower mass loss within the 15-h test duration was shown by the samples having a thick modified layer consisting of expanded austenite with a low amount of nitrides and/or carbides. On the contrary, the presence of a high content of brittle carbides increased significantly mass loss, and the erosion rate was higher than that of the untreated alloy.

The formation of a γ_N layer improves corrosion resistance in Cl^--containing solutions. Nitrided ASTM F75 had the same passive behavior of the untreated alloy, but it showed an increase in corrosion potential and pitting potential and a decrease in passive current density when tested in NaCl solution [173] and Hank's solution [172, 173]. Higher OCP values were also registered [173]. Corrosion current density and anodic current density values increased when nitride precipitates were present [172, 173]. An increase in corrosion resistance was also observed for plasma nitrided UNS R31538 tested in Ringer's solution [28] (Figure 7a). Similarly, a γ_C layer has an enhanced corrosion resistance especially in NaCl solutions and in solution simulating body fluids. A shift in the polarization curves, typical of a metal with a passive behavior, toward nobler potential values and lower anodic current density were registered for plasma carburized Stellite 21, tested in 3.5 wt.% NaCl [166]. An increase in OCP values and corrosion potential and a decrease in the current density in the passive branch were observed in Ringer's solution for carburized UNS R31537 [59, 84] and UNS R31538 [171] (Figure 7b). EIS analysis on similar specimens

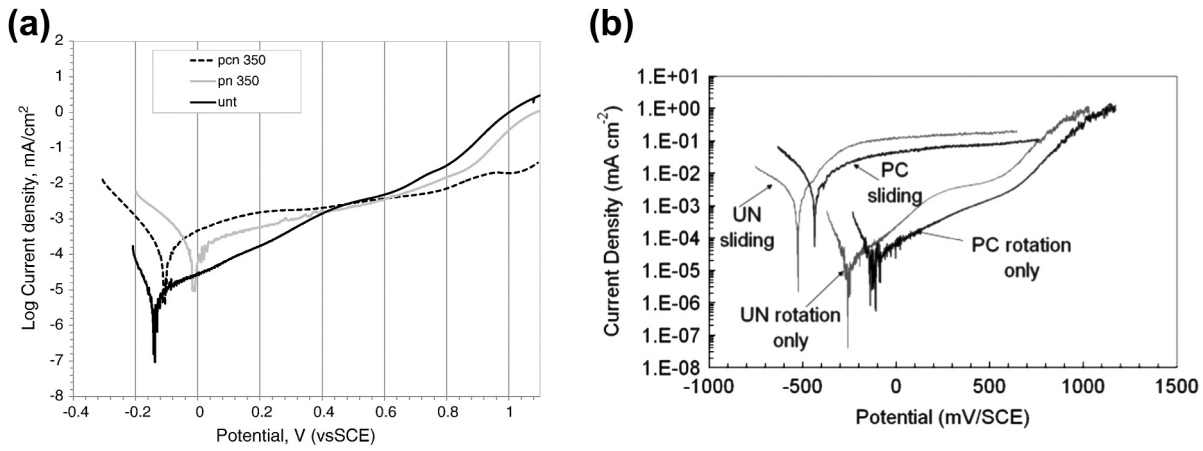

FIGURE 7 | Potentiodynamic polarization curves of untreated (unt), nitrided (350°C) (pn 350) and nitrocarburized (350°C) (pcn 350) Co-28Cr-6Mo UNS R31538 (reproduced from ref. [28] under the terms of CC-BY license. Copyright 2013 by the authors) (a), and of untreated (UN) and carburized (450°C) (PC) Co-28Cr-6Mo UNS R31538 tested under sliding (tribocorrosion) and rotation only (corrosion) conditions (reproduced from ref. [171], copyright 2013, with permission from Elsevier) (b). (Solution: Ringer's solution).

tested in Ringer's solution highlighted that the passive film of the carburized specimens had a higher polarization resistance, if compared to that of the untreated alloy [169]. When carbides formed in the modified layer, as when treatments were performed at higher temperatures, a decrease in corrosion resistance was reported [166]. Corrosion resistance was also improved in plasma nitrocarburized UNS R31538 when tested in Ringer's solution [28] (Figure 7a).

For the biomedical grades, the assessment of the biocompatibility of the surface treated samples is of paramount importance. Citocompatibility evaluation of gaseous carburized UNS R31537 put in contact in vitro with human fetal osteoblasts showed that the treated samples were as cytocompatible as the untreated alloy [84].

Low-temperature nitriding also influences the magnetic behavior. The ε-Co hcp phase has a ferromagnetic behavior, while the α-Co fcc phase is nonmagnetic [178]. It was shown that γ_N formed on paramagnetic Co-Cr-Mo ISO 5832-12 alloy had a ferromagnetic behavior [58, 77]. The magnetic domains had different patterns from one grain to another, probably due to different N content and lattice expansion, and even within the single grain [58], and their size increased as the treatment duration was longer [77]. The characteristics of the magnetic domains depend also on phase composition. When the γ_N layer was thin and discontinuous, indistinct magnetic domains with weak magnetic contrast were observed [58], while strong magnetic contrast was detected when a thick, N-rich γ_N layer was present and when CrN formed precipitates within the γ_N matrix. As more Cr nitrides formed and γ_N decomposed into a low-N Cr-depleted (Co, Mo) fcc phase, weak magnetic contrast was again registered [58]. Magneto-optic Kerr effect (MOKE) analysis confirmed the ferromagnetic type behavior [77]. Specimens nitrided at 400°C for durations ranging from 1 to 20 h showed a loop behavior with a relatively small coercivity, similar to that of a soft ferromagnet [77]. It was hypothesized that this ferromagnetic state is related to the fairly large lattice expansion (~10%) of the fcc lattice, which influences the electronic structure reducing the 3*d*-3*d* orbitals overlap, thus enhancing Co magnetic moment [58, 77].

7 | Entropy Alloy

Entropy alloys are multicomponent alloys that have gained increasing attention in recent years, due to many favorable properties, such as high strength and fracture toughness, corrosion and oxidation resistance [73, 179, 180]. The new alloy design concept is based on mixing together multiple principal alloy elements, instead of a primary element with secondary additions, which is the basis of "conventional" alloy systems. The mixing entropy of a multicomponent alloy tends to hinder the precipitation of intermetallics and stabilizes a solid-solution-like structure, so that even a single phase can be obtained. The mixing of multiple components has four "core effects," the high mixing entropy, which promotes a stable structure, the lattice distortion, which is accounted for the improvement in hardness and strength, the sluggish diffusion of substitutional atoms, which enhances thermal stability and the resistance to oxidation and corrosion, and the synergetic cocktail effect [73]. Entropy alloys are classified in medium (MEA) and high (HEA), depending on the mixing entropy amount, the number of components, and their amount [73, 180]. An extended use of these alloys for demanding applications requires a further improvement in wear and corrosion resistance, and hence the possibility of N and/or C alloying at the surface [50] or in the bulk [181] has been explored. Regarding surface treatment studies, most of them employ fairly high treatment temperatures, causing the formation of compounds [50], or they are focused on the production of high-entropy nitrides [73]. Only recently the possibility of applying low-temperature thermochemical treatments has begun to be explored for a few medium- and high-entropy alloys, as reported in Table 6. In the table, the different alloy types are classified using the entropy criterion, regardless of the designation of the authors.

Low-temperature nitriding treatments have been applied on both medium- and high-entropy alloys using plasma-based processes. In particular, the use of an active screen may produce a topmost layer due to the recondensation of nanometer nitrides formed from the sputtering of the screen material [60, 183, 184]. These nitrides alter the typical surface morphology observed in low-temperature nitrided alloys. When the treated surface is free from nitride particles, the swelling of the grains was observed [30, 182, 185]. The microscopy analysis of the cross-section showed the formation of a continuous modified layer well resistant to chemical etching [30, 31, 182] (Figure 8a). Micro-cracks may occur when a large N content is solubilized, as it was observed in $FeCrNiSi_{0.5}$ alloy nitrided at 430°C, for which a N content in the range 30–43 at.% was registered in the first 5 μm [60], suggesting a brittle behavior due to the high residual stress. In $FeCrNiSi_{0.5}$ [60] and CoCrFeNi [31], TEM analysis highlighted the presence of shear bands, due to the local plastic deformations occurring with the formation of γ_N. It has to be noted that the fairly high SFE of these medium-entropy alloys hinders the formation of extended stacking faults, and hence the formation of N-rich hcp ε_N' martensite [31]. The formation of a MN (M = Cr + other alloy elements) nitride having a NaCl-type lattice, analog to CrN, was observed as treatment temperature and/or time were increased [31, 182, 186]. However, alloy composition also plays a role in nitride formation. MN nitride was observed together with γ_N in CoCrFeNiTi nitrided at 400°C [184], nano-sized CrN dots were detected in $FeCrNiSi_{0.5}$ treated at 430°C [60], while CrN was observable in CoCrFeNi [31], $Fe_{40}Mn_{20}Cr_{20}Ni_{20}$ [182], $CoCrFeNiMo_{0.2}$ [183] and CoCrFeMnNi [30] specimens nitrided at 450°C or higher. A nitride-rich nanocrystalline region was also detected as a topmost layer [31, 60]. When nitriding was carried out at higher temperatures, γ_N tended to decompose, and its transformation into CrN + low-Cr γ [31, 182], CrN + low-Cr γ + bcc α [60], and CrN + ε-M_3N + bcc α [183] was observed. The importance of alloy composition in γ_N transformation can be highlighted by the comparison of two studies. Using the same treatment conditions (480°C, 10 h), in CoCrFeNi, a complex

TABLE 6 | Medium- (MEA) and high- (HEA) entropy alloy types subjected to low-temperature thermochemical treatments.

Alloy type	Composition (at.%)	Treatment type	References
$FeCrNiSi_{0.5}$ (MEA)	Fe: 26.4; Cr: 34.3; Ni: 29.9; Si: 9.4	Active-screen plasma nitriding (T: 430–480°C; t: 10 h)	[60]
$Fe_{40}Mn_{20}Cr_{20}Ni_{20}$ (MEA)	Fe: 40; Cr: 20; Mn: 20; Ni: 20	Plasma nitriding (T: 400–600°C; t: 2–10 h)	[182]
CoCrFeNi (MEA)	Co: 25; Cr: 25; Fe: 25; Ni: 25	Active-screen plasma nitriding (T: 430–480°C; t: 10 h)	[31]
		Gaseous carburizing (T: 470°C; t: 40 h)	[85]
		Gaseous nitrocarburizing (unspecified)	[88]
$Al_{0.1}CoCrFeNi$ (MEA)	Al: 2.4; Co: 24.4; Cr: 24.4; Fe: 24.4; Ni: 24.4	Gaseous carburizing (T: 470°C; t: 30 h)	[61]
$Al_{0.5}CoCrFeNi$ (HEA)	Al: 11.1; Co: 22.2; Cr: 22.2; Fe: 22.2; Ni: 22.2	Gaseous carburizing (T: 470°C; t: 30 h)	[61]
$CoCrFeNiMo_{0.2}$ (HEA)	Co: 22.9; Cr:23.7; Fe: 23.8; Ni: 24.0; Mo: 5.6	Active-screen plasma nitriding (T: 400–500°C; t: 10 h)	[183]
CoCrFeNiTi (HEA)	Co: 20; Cr: 20; Fe: 20; Ni: 20; Ti: 20	Auxiliary cathode screen-d.c. plasma nitriding (T: 400–600°C; t: 15 h)	[184]
CoCrFeMnNi (Cantor alloy) (HEA)	Co: 20; Cr: 20; Fe: 20; Mn: 20; Ni: 20	Auxiliary cathode screen-d.c plasma nitriding (T: 400–550°C; t: 15 h)	[30, 185]
		Gaseous nitrocarburizing (unspecified)	[88]
CoCrCuFeNi (HEA)	Co: 20; Cr: 20; Cu: 20; Fe: 20; Ni: 20	Plasma nitriding with/without lanthanum addition (T: 440°C; t: 8–24 h)	[186]

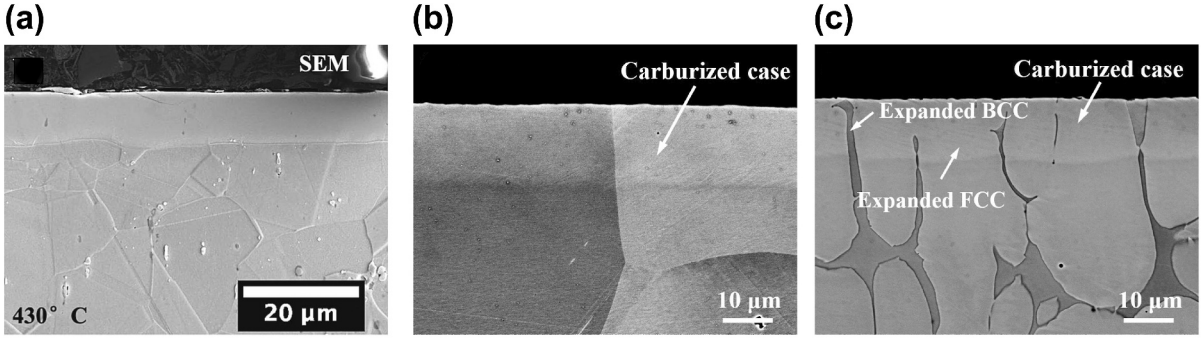

FIGURE 8 | Cross-section micrograph of nitrided (430°C) CoCrFeNi (reproduced from ref. [31] under the terms of CC-BY license. Copyright 2024 by the authors) (a), and carburized (470°C) $Al_{0.1}CoCrFeNi$ (b) and $Al_{0.5}CoCrFeNi$ (c) (reproduced from ref. [61], copyright 2023, with permission from Elsevier).

structure formed, consisting of CrN nano-lamellae at grain boundary and nano-dots within γ_N [31], while in $FeCrNiSi_{0.5}$ Si-rich $(Cr,Si)_xN$ nano-precipitates alone were detected, suggesting that, thanks to Si, Cr segregation was slowed down [60]. A more or less continuous layer of MN, maintaining the same composition of the matrix, was inferred in CoCrFeMnNi alloy nitrided at 500 and 550°C [30]. The thickness of the modified layer increases as the treatment temperature is higher [30, 31, 60, 183–185], or as treatment duration is longer [186]. The use of lanthanum (La) rare-earth addition in the plasma-nitriding step promoted the formation of thicker modified layers [186]. It was hypothesized that, entering in the surface layers, La atoms form anti-trapping regions, and hence accelerate the diffusion of N atoms by reducing the activation energy for this process.

The N content profile has the typical step-like trend [30, 31, 60, 183–185]. Both maximum N content and N content in the plateau-like zone depend on the alloy composition. As an example, in nitrided (430°C, 10 h) $FeCrNiSi_{0.5}$ alloy a maximum N content of 38–43 at.% was registered near the surface, and 30–36 at.% in the plateau zone [60]. However, when CoCrFeNi alloy was treated in the same conditions, a maximum N content of 30–33 at.% was detected, followed by a plateau in the range of 20–28 at.% [31] It has to be noted that, despite the increase in Cr content if compared to that of austenitic stainless steels, the maximum N content in CoCrFeNi alloy reaches slightly lower values, suggesting that the addition of large amounts of Ni and Co tends to hinder the effect of Cr on N uptake [31]. The peculiar composition of CoCrFeNi alloy also has effects on the modified layer thickness. While in Co-Cr and Ni-Cr alloys thinner modified layers are produced, if compared to those obtained in austenitic stainless steels using comparable treatment conditions, thicker layers were observed in CoCrFeNi. As an example, using an active-screen plasma nitriding treatment (430–480°C, 10 h), the thickness of the modified layer ranged ~9–16 μm for CoCrFeNi alloy [31], while for AISI 316 ranged ~8–13 μm [60]. When the $FeCrNiSi_{0.5}$ alloy is considered, the modified layer thickness was comparable to that obtained in AISI 316 [60]. It has to be hypothesized that the peculiar composition of the CoCrFeNi alloy is able to promote the diffusion of interstitial atoms, while the diffusion of substitutional atoms remains sluggish.

Low-temperature carburizing was studied on CoCrFeNi alloy [85] and its modifications adding Al [61]. In the carburized CoCrFeNi, a C-rich supersaturated fcc solid solution easily formed, while carbides were not detected [85]. When a low Al content was added to the base alloy, as in $Al_{0.1}$CoCrFeNi, the fcc matrix structure was retained and the carburizing treatment allowed for producing a continuous γ_C layer [61] (Figure 8b), analogous to that observed in the Al-free alloy. As the Al content was increased, as in $Al_{0.5}$CoCrFeNi, the untreated alloy consisted of fcc grains with a minor amount of interdendritic Al- and Ni-rich bcc phase. Low-temperature carburizing allowed for the formation of γ_C together with an expanded bcc phase, which was indicated as expanded martensite [61] (Figure 8c). A partial transformation of the bcc phase into γ_C was detected, and carbides were not observed. In the cross-section, the modified layer consisted of γ_C grains interspersed with C-rich bcc grains, similarly to what is observed for low-temperature treated duplex stainless steels, in which both expanded austenite and expanded ferrite form [10]. A thicker modified layer (~16 μm) was obtained in the low-Al alloy, while in the high-Al alloy a thinner (~10 μm) carburized case was produced. A maximum C content of 3 wt.% (~12.7 at.%) was measured at the surface of carburized CoCrFeNi alloy [85]. Al addition also influenced the C content: a maximum C content of ~13 at.% was registered in the $Al_{0.1}$CoCrFeNi alloy, while for the $Al_{0.5}$CoCrFeNi alloy the maximum C content was ~11 at.% [61].

The effects of low-temperature nitrocarburizing were studied on CoCrFeNi and CoCrFeMnNi alloys [88]. A fairly homogeneous modified layer formed, which consisted of γ_N and γ_C and had a strong resistance to chemical etching. The N and C profiles showed a N-rich layer near the surface, followed by a thicker C-rich layer. The thicknesses of the N-rich layer for the two alloys were comparable, but a thicker C-rich layer was registered in CoCrFeMnNi than that produced in CoCrFeNi alloy.

Low-temperature nitriding produces hardened surface layers, reaching values of ~12.7 GPa [30]. The microhardness profile has the typical step-like trend, with a more or less extended region of high hardness values near the surface, followed by a steep decrease to matrix values [30, 184]. A smoother trend was observed when La was added in plasma nitriding treatment [186]. Microhardness profiles of carburized CoCrFeNi alloy are fairly smooth, similar to the C profile [85]. Values as high as ~12 GPa were measured at the surface, ~5 times higher than the substrate [85]. It has to be noted that these hardness values are higher than that obtained for the same alloy with high-temperature carburizing, in which carbides were produced [187]. When Al was added, for the $Al_{0.1}$CoCrFeNi alloy the hardness at the surface was ~12.9 GPa, followed by a smooth decrease to matrix values (~2.8 GPa) [61]. For the $Al_{0.5}$CoCrFeNi alloy, the maximum hardness value in the γ_C grains was lower, 11.9 GPa, and a similar trend of the hardness profile was registered. Regarding the bcc phase, in the untreated alloy it had a significantly higher hardness value (7.8 GPa) than the fcc phase (3.9 GPa). C enrichment caused only a minor hardness increase, from 7.8 to ~10.3 GPa [61]. If compared to nitriding treatment, the nitrocarburizing treatments produce smoother hardness profiles, in which a gradual decrease from ~12.8 GPa to matrix value (< 4 GPa) was observed [88].

Low-temperature nitriding allows for an enhancement in wear resistance. A significant decrease in wear loss was registered when the treated specimens had duplex layers, consisting of a nitride-rich layer, deposited by means of active-screen process, on a γ_N layer [183], γ_N layers with/without nitrides [30, 185], and γ_N layers produced by nitriding with La addition [186]. The transformation of γ_N into CrN and low-N γ, as obtained at high treatment temperatures, improved the sliding wear resistance from room temperature up to 600°C [182]. A significant enhancement in wear resistance was also obtained thanks to nitrocarburizing treatments [88].

The study of the corrosion behavior of nitrided entropy alloys has often been biased by the formation of a deposited layer due to the use of active-screen processes. As a matter of fact, when a

nitride-free modified layer forms, a higher pitting potential was observed [30, 183, 185] and the γ_N surface was fairly unetched when tests were carried out in NaCl solution [183]. The presence of a small amount of nitride precipitates did not significantly affect corrosion resistance [183, 185, 186], but, as the content increased, corrosion resistance worsened [30, 183, 184]. The formation of γ_N and γ_C, produced with nitrocarburizing treatment, also influences corrosion behavior. When potentiodynamic tests were carried out in a NaCl solution, the anodic current density of the treated samples had a lower gradient than that of the untreated alloys and an increase in pitting potential was registered [88]. However, when tested in a 0.05 M H_2SO_4 solution, the nitrocarburized samples showed higher anodic current densities in the passive branch than those of the untreated alloys, suggesting a worsening of the corrosion resistance [88].

8 | Expanded Austenite and the Role of Alloy Elements: Some Considerations

This overview on thermochemical treatments performed at low-temperature has shown that N- and/or C-rich expanded austenite can be produced on different fcc alloys. A relevant role in promoting the formation of this supersaturated solid solution has usually been assigned to Cr, and often it has been indicated as the indispensable alloy element for forming expanded austenite. As a matter of fact, the research studies have shown that a solid solution in the fcc lattice having an interstitial (especially, N) content larger than that at equilibrium conditions can be obtained in many Cr-free alloys, such as Fe-Ni Invar [128, 134], Fe-24Mn-2Al-0.45C TWIP steel [135], Ni-Ti [52, 141, 142], Ni-Nb [52, 141], Ni-V [52, 141] and Ni-Mn [52, 141] alloys. Therefore, it may be supposed that the conditions which promote the formation of expanded austenite are related more to a "chemical environment" than strictly to an atom type. Considering both the experimental and simulation data, the formation of a preferential bond between a metal atom with N or C seems a necessary condition for the entrapment of interstitials in the metal fcc lattice. The "trapping" effect of Cr toward N and C is well known [101, 129, 188], but a preferential bond of Fe with N was also suggested [97], so that the formation of γ_N in Fe-Ni alloys can be explained. Regarding N-rich expanded austenite, the trapping effect of different metal atoms can be evaluated considering the N-metal interactions in forming MN fcc-based nitrides [72, 189]. When M is a transition metal, the bond between M and N is a mixture of metallic, covalent and ionic components [72, 189]. The tendency to form a strong bond and thermodynamically stable nitrides varies along the periodic table and tends to decrease from Group 4 to 11, with strong nitride formers in the Group 4 (Ti), 5 (V, Nb) and 6 (Cr, Mo), weak nitride formers in groups 7 (Mn), 8 (Fe), 9 (Co), 10 (Ni), while for Cu, in Group 11, the formation of a MN-type nitride is not reported [72, 189]. Therefore, Cr can form fairly strong bonds and entrap N in the octahedral interstitial site. However, bonds can also be exerted by Mn and Fe, even if weaker but sufficient to maintain N in solid solution, while Ni and Co seem unable to entrap N. Regarding Ti, V and Nb, they have a stronger interaction with N than Cr, and therefore their nitrides may easily precipitate. Together with transition metals, Al and Si are often used as alloy elements. Both Al and Si are strong nitride formers, but their bonding with N is covalent [189]. In Ni binary alloys, they are not able to entrap significant amounts of N [52, 141], suggesting that it is not the strength of the M-N interaction alone to promote the formation of expanded austenite. In Ni superalloys, the importance of the "chemical environment" has been highlighted by first-principles calculations regarding the solubilization of N in γ'-Ni_3Al precipitates [159]. As recalled above, N atoms prefer to occupy the larger interstitial sites surrounded by six Ni atoms, than the smaller ones surrounded by both Ni and Al atoms, although Al-N interaction is stronger than Ni-N bond. However, the effect of strong nitride forming elements as Ti, Nb, Al and Si has to be considered when the formation of Cr nitrides should be hindered for preserving corrosion resistance. A favorable "chemical environment" is also required for C-rich expanded austenite, and the tendency of transition metals to form bonds with C is similar to that observed for N [72].

The analysis of the reviewed studies suggests that a balance between "trapping" and "untrapping" elements is important for both the diffusion kinetics and the interstitial solubilization of N and C atoms in the para-equilibrium conditions of low-temperature treatments. Entropy alloys are particularly promising as a basis for studying the effects of metals having strong or weak interactions with N/C in promoting the formation of expanded austenite. The use of different metal atom mixtures can be useful to investigate the influence of alloy elements on the diffusion kinetics of interstitial atoms in the fcc lattice and assess the conditions for the formation of expanded austenite without/with other phases (martensitic phases, nitrides, carbides, intermetallic precipitates), as well as to study the effects of different metal elements on the characteristics of the modified layer in view of producing surface treated components with required characteristics. As an example, Mn seems a promising candidate for promoting N solubilization, but it can also cause a decrease in SFE, so that a fcc-to-hcp martensitic transformation may occur. As reported in Section 3, in austenitic stainless steels the presence of ε_N' martensite seems to promote the load bearing capacity of the nitrided specimens [109] and it does not adversely affect the enhanced corrosion resistance of the γ_N layer in NaCl solutions [16, 102, 109], but it can cause a significant worsening of corrosion resistance in H_2SO_4 solutions [102], and therefore a careful choice of steel composition and treatment conditions should be made according to the service environment. Moreover, low-temperature treatments may elucidate the effects of the solubilization of an interstitials concentration comparable to that of metal atoms on the peculiar characteristics of entropy alloys.

The presence of different alloy elements affects not only the characteristics of the modified layer, but also those of the passive layer formed on it. At present, only the passive layer formed on expanded austenite in austenitic stainless steel has been extensively investigated [9, 15]. The study of the characteristics of the passive film, the eventual presence of an N- or C-rich region inside the film and its influence on corrosion phenomena, as well as of the effects of the presence of other phases together with expanded austenite, is important for optimizing the surface treatments for the mitigation of corrosion in different environments.

Another characteristic which is influenced by alloy elements is the magnetic behavior. Alloy composition affects the interstitials content, lattice expansion and atom separation, and hence the magnetic behavior. The studies on this topic were concentrated especially on austenitic stainless steels [11], and only a nitrided Co-Cr-Mo alloy was studied [58, 77] among the other alloy types. The assessment of the conditions for forming a ferromagnetic layer and the study of the characteristics of the ferromagnetic expanded austenite as a function of alloy content and interstitials concentration have important technological implications, such as the creation of magnetic devices, since magnetic patterns on a paramagnetic substrate can be easily obtained performing the surface treatment using a mask [190], and the possible use of low-temperature treatments for biomedical applications.

9 | Conclusions and Outlooks

Thermochemical treatments performed at low temperatures are effective in forming N and/or C expanded austenite in a variety of fcc alloys, from austenitic stainless steels to Ni and Co alloys, to entropy alloys. The characteristics of this phase and of the modified surface layers in which it is present tend to remain similar, irrespectively of the alloy type, although the change in alloy composition is able to modulate the modified layer formation and properties. The solid solution of interstitial atoms well beyond the solubility limit promotes surface hardness by a combination of solid solution strengthening, strain hardening and compressive residual stress, and hence tribological properties and fatigue resistance can be improved. The solubilization of N and C is effective in enhancing corrosion resistance in Cl^--ion containing environments, while in Cl^--free environments, such as in H_2SO_4 solutions, the corrosion behavior is influenced by the concurrent presence of other phases, such as martensitic phases or compound precipitates. The expansion of the fcc lattice and the change in electronic environment affect magnetic properties, so that a soft ferromagnetic layer on a non-magnetic matrix can be obtained. All these characteristics allow to extend the applications of the treated alloys in many industrial fields. However, surface engineering should enable the production of modified surface layers optimized for specific applications, and hence a thorough knowledge of the surface treatments-microstructure-properties relationships is needed. As a matter of fact, while the formation conditions and many properties of expanded austenite are well assessed for austenitic stainless steels, they are not fully explored for the other fcc alloys and many questions are still open, which can be the basis for future research activities. The review of international literature has highlighted that not only the treatment conditions but also the chemical composition of the alloy (element type, concentration) influence the diffusion kinetics of the interstitial atoms and their solubilization in expanded austenite, and hence the produced N and/or C concentration profile, which affects many properties of the modified layer. Experimental and simulation studies can help to elucidate this aspect, as well as the dependence of the characteristics and properties of expanded austenite and the modified layer on the substrate type. These studies can be relevant from a technological point of view, since they can be useful to identify the treatment conditions and suitable alloys for obtaining modified surface layers with optimized characteristics, tailored for specific service environments. The development of new alloys, both "conventional" and entropy types, suitable for low-temperature treatments can also be stimulated.

Acknowledgments

Open access publishing facilitated by Universita degli Studi di Firenze, as part of the Wiley - CRUI-CARE agreement.

Conflicts of Interest

The author declares no conflicts of interest.

Data Availability Statement

The data that support the findings of this study are available on request from the corresponding author. The data are not publicly available due to editorial restrictions.

References

1. T. Burakowski and T. Wierzchoń, *Surface Engineering of Metals* (CRC Press, 2020). ISBN 9780367400125.

2. M. Ramezani, Z. Mohd Ripin, T. Pasang, and C.-P. Jiang, "Surface Engineering of Metals: Techniques, Characterizations and Applications," *Metals* 13 (2023): 1299, https://doi.org/10.3390/met13071299.

3. F. Czerwinski, "Thermochemical Treatment of Metals," in *Heat Treatment - Conventional and Novel Applications*, ed. F. Czerwinski (IntechOpen, 2012), 73–112. ISBN 978-953-51-0768-2, https://doi.org/10.5772/51566.

4. J. M. O'Brien and D. Goodman, "Plasma (Ion) Nitriding," in *ASM Handbook*, Vol. 4 (ASM International, 1997), 420–424.

5. B. Edenhofer, D. Joritz, M. Rink, and K. Voges, "Carburizing of Steels," in *Thermochemical Surface Engineering of Steels*, ed. E. J. Mittemeijer and M. A. J. Somers (Woodhead Publishing, 2015), 485–553. ISBN 978-0-85709-592-3, https://doi.org/10.1533/9780857096524.3.485.

6. J. Sun, H. Tang, C. Wang, Z. Han, and S. Li, "Effects of Alloying Elements and Microstructure on Stainless Steel Corrosion: A Review," *Steel Research International* 93 (2022): 2100450, https://doi.org/10.1002/srin.202100450.

7. M. A. J. Somers and T. L. Christiansen, "Low Temperature Surface Hardening of Stainless Steel," in *Thermochemical Surface Engineering of Steels*, ed. E. J. Mittemeijer and M. A. J. Somers (Woodhead Publishing, 2015), 557–579. ISBN 978-0-85709-592-3, https://doi.org/10.1533/9780857096524.4.557.

8. G. M. Michal, F. Ernst, H. Kahn, et al., "Carbon Supersaturation due to Paraequilibrium Carburization: Stainless Steels With Greatly Improved Mechanical Properties," *Acta Materialia* 54 (2006): 1597–1606, https://doi.org/10.1016/j.actamat.2005.11.029.

9. F. Borgioli, "The Expanded Phases Formed in Stainless Steels by Means of Low-Temperature Thermochemical Treatments: A Corrosion Perspective," *Metals* 14 (2024): 1371, https://doi.org/10.3390/met14121371.

10. F. Borgioli, "The "Expanded" Phases in the Low-Temperature Treated Stainless Steels: A Review," *Metals* 12 (2022): 331, https://doi.org/10.3390/met12020331.

11. F. Borgioli, "From Austenitic Stainless Steel to Expanded Austenite-S Phase: Formation, Characteristics and Properties of an Elusive Metastable Phase," *Metals* 10 (2020): 187, https://doi.org/10.3390/met10020187.

12. Y. Sun and R. Bailey, "Comparison of Wear Performance of Low Temperature Nitrided and Carburized 316L Stainless Steel Under Dry Sliding and Corrosive-Wear Conditions," *Journal of Materials Engineering and Performance* 32 (2023): 1238–1247, https://doi.org/10.1007/s11665-022-07182-9.

13. Z. Liu, S. Wang, Y. Feng, X. Wang, Y. Peng, and J. Gong, "Exploration on the Fatigue Behavior of low-Temperature Carburized 316L Austenitic Stainless Steel at Elevated Temperature," *Materials Science and Engineering: A* 850 (2022): 143562, https://doi.org/10.1016/j.msea.2022.143562.

14. K. S. Wang, H. L. Che, and M. K. Lei, "Corrosion-Fatigue Properties of Plasma-Based low-Energy Nitrogen Ion Implanted AISI 304L Austenitic Stainless Steel in Borate Buffer Solution," *Surface and Coatings Technology* 288 (2016): 30–35, https://doi.org/10.1016/j.surfcoat.2016.01.010.

15. F. Borgioli, "The Corrosion Behavior in Different Environments of Austenitic Stainless Steels Subjected to Thermochemical Surface Treatments at Low Temperatures: An Overview," *Metals* 13 (2023): 776, https://doi.org/10.3390/met13040776.

16. F. Borgioli, E. Galvanetto, and T. Bacci, "Corrosion Behaviour of Low Temperature Nitrided Nickel-Free, AISI 200 and AISI 300 Series Austenitic Stainless Steels in NaCl Solution," *Corrosion Science* 136 (2018): 352–365, https://doi.org/10.1016/j.corsci.2018.03.026.

17. G. Maistro, S. Kante, L. Nyborg, and Y. Cao, "Low-Temperature Carburized High-Alloyed Austenitic Stainless Steels in PEMFC Cathodic Environment," *Surfaces and Interfaces* 24 (2021): 101093, https://doi.org/10.1016/j.surfin.2021.101093.

18. M. Stio, M. Martinesi, C. Treves, and F. Borgioli, "Cultures and Co-Cultures of Human Blood Mononuclear Cells and Endothelial Cells for the Biocompatibility Assessment of Surface Modified AISI 316L Austenitic Stainless Steel," *Materials Science and Engineering: C* 69 (2016): 1081–1091, https://doi.org/10.1016/j.msec.2016.08.010.

19. J. Buhagiar, T. Bell, R. Sammons, and H. Dong, "Evaluation of the Biocompatibility of S-Phase Layers on Medical Grade Austenitic Stainless Steels," *Journal of Materials Science: Materials in Medicine* 22 (2011): 1269–1278, https://doi.org/10.1007/s10856-011-4298-3.

20. F. Borgioli, E. Galvanetto, and T. Bacci, "Influence of Surface Morphology and Roughness on Water Wetting Properties of Low Temperature Nitrided Austenitic Stainless Steels," *Materials Characterization* 95 (2014): 278–284, https://doi.org/10.1016/j.matchar.2014.07.006.

21. F. Borgioli, E. Galvanetto, and T. Bacci, "Effects of Surface Modification by Means of Low Temperature Plasma Nitriding on Wetting and Corrosion Behavior of Austenitic Stainless Steel," *Coatings* 10 (2020): 98, https://doi.org/10.3390/coatings10020098.

22. T. Czerwiec, S. Tsareva, A. Andrieux, S. Bruyère, and G. Marcos, "Effects of Surface Topography at Different Scales on the Dispersion of the Wetting Data for Sessile Water Droplets on Nitrided Austenitic Stainless Steels," *Surface and Coatings Technology* 441 (2022): 128510, https://doi.org/10.1016/j.surfcoat.2022.128510.

23. B. K. Brink, K. Ståhl, T. L. Christiansen, C. Frandsen, M. F. Hansen, and M. A. J. Somers, "Composition-Dependent Variation of Magnetic Properties and Interstitial Ordering in Homogeneous Expanded Austenite," *Acta Materialia* 106 (2016): 32–39, https://doi.org/10.1016/j.actamat.2015.12.043.

24. P. Schuler, U. Krupp, P. Gümpel, J. Mayer, A. Schwedt, and A. Aretz, "Investigation of Alloy-Dependent Occurrence of Ferromagnetism in Carbon-Expanded Austenitic Steel After Low-Temperature Surface Hardening," *Steel Research International* 92 (2021): 2100272, https://doi.org/10.1002/srin.202100272.

25. H. S. Dong, "Phase Surface Engineering of Fe-Cr, Co-Cr and Ni-Cr Alloys," *International Materials Reviews* 55 (2010): 65–98, https://doi.org/10.1179/095066009X12572530170589.

26. S. Chollet, L. Pichon, J. Cormier, et al., "Plasma Assisted Nitriding of Ni-Based Superalloys With Various Microstructures," *Surface and Coatings Technology* 235 (2013): 318–325, https://doi.org/10.1016/j.surfcoat.2013.07.060.

27. O. P. Calabokis, Y. E. Nuñez de la Rosa, V. Ballesteros-Ballesteros, and E. A. Gil González, "Nitriding Treatments in Nickel–Chromium-Based Superalloy INCONEL 718: A Review," *Coatings* 14 (2024): 993, https://doi.org/10.3390/coatings14080993.

28. R. Liu, X. Li, X. Hu, and H. Dong, "Surface Modification of a Medical Grade Co-Cr-Mo Alloy by low-Temperature Plasma Surface Alloying With Nitrogen and Carbon," *Surface and Coatings Technology* 232 (2013): 906–911, https://doi.org/10.1016/j.surfcoat.2013.06.122.

29. T. Aizawa, T. Funazuka, T. Shiratori, and Y. Suzuki, "Massive Nitrogen Supersaturation to CoCrMo Alloys for Surface Microstructure Control," *Academia Materials Science* 1 (2023), https://doi.org/10.20935/AcadMatSci6139.

30. A. Nishimoto, T. Fukube, and T. Maruyama, "Microstructural, Mechanical, and Corrosion Properties of Plasma-Nitrided CoCrFeMnNi High-Entropy Alloys," *Surface and Coatings Technology* 376 (2019): 52–58, https://doi.org/10.1016/j.surfcoat.2018.06.088.

31. X. Tao, Y. Yang, J. Qi, et al., "An Investigation on Nitrogen Uptake and Microstructure of Equimolar Quaternary FeCoNiCr High Entropy Alloy After Active-Screen Plasma Nitriding," *Materials Characterization* 208 (2024): 113593, https://doi.org/10.1016/j.matchar.2023.113593.

32. M. A. J. Somers and T. L. Christiansen, "Gaseous Processes for Low Temperature Surface Hardening of Stainless Steel," in *Thermochemical Surface Engineering of Steels*, ed. E. J. Mittemeijer and M. A. J. Somers (Woodhead Publishing, 2015), 581–614. ISBN 978-0-85709-592-3, https://doi.org/10.1533/9780857096524.4.581.

33. T. Christiansen and M. A. J. Somers, "Low Temperature Gaseous Nitriding and Carburising of Stainless Steel," *Surface Engineering* 21 (2005): 445–455, https://doi.org/10.1179/174329405X68597.

34. J. P. Lebrun, "Plasma-Assisted Processes for Surface Hardening of Stainless Steel," in *Thermochemical Surface Engineering of Steels*, ed. E. J. Mittemeijer and M. A. J. Somers (Woodhead Publishing, 2015), 615–632. ISBN 978-0-85709-592-3, https://doi.org/10.1533/9780857096524.4.615.

35. B. C. E. Schibicheski Kurelo, G. B. De Souza, S. L. Da Silva, et al., "Tribo-Mechanical Behavior of Films and Modified Layers Produced by Cathodic Cage and Glow Discharge Plasma Nitriding Techniques," *Metals* 13 (2023): 430, https://doi.org/10.3390/met13020430.

36. V. Tandon, A. P. Patil, and R. C. Rathod, "Influence of Time on Low Temperature Salt Bath Nitriding and Its Corrosion Behavior of 316L ASS in PEMFC Environment," *Protection of Metals and Physical Chemistry of Surfaces* 56 (2020): 772–779, https://doi.org/10.1134/S2070205120040243.

37. H. Markanday, S. C. Roy, and M. A. J. Somers, "On the Effect of Salt Bath Nitrocarburizing on the Cavitation Erosion Behavior of AISI 304L Stainless Steel," *Engineering Failure Analysis* 165 (2024): 108752, https://doi.org/10.1016/j.engfailanal.2024.108752.

38. C. Illing, Z. Ren, A. Agaponova, A. Heuer, and F. Ernst, "Rapid Alloy Surface Engineering Through Closed-Vessel Reagent Pyrolysis," *Metals* 11 (2021): 1764, https://doi.org/10.3390/met11111764.

39. M. A. J. Somers and T. L. Christiansen, "Low-Temperature Surface Hardening of Stainless Steel," in *ASM Handbook*, ed. J. L. Dossett and G. E. Totten, Vol. 4D (ASM International, 2014), 439–450. ISBN 978-1-62708-168-9, https://doi.org/10.31399/asm.hb.v04d.a0005959.

40. S. R. Collins, P. C. Williams, S. V. Marx, A. Heuer, F. Ernst, and H. Kahn, "Low-Temperature Carburization of Austenitic Stainless Steels," in *ASM Handbook*, ed. J. Dosset and G. E. Totten, Vol. 4D (ASM International, 2014), 451–460. ISBN 978-1-62708-168-9, https://doi.org/10.31399/asm.hb.v04d.a0005939.

41. T. Bell, "Current Status of Supersaturated Surface Engineered S-Phase Materials," *Key Engineering Materials* 373–374 (2008): 289–295, https://doi.org/10.4028/www.scientific.net/KEM.373-374.289.

42. L. C. Casteletti, A. L. Neto, and G. E. Totten, "Nitriding of Stainless Steels," *Metallography, Microstructure and Analysis* 3 (2014): 477–508, https://doi.org/10.1007/s13632-014-0170-4.

43. T. Czerwiec, H. He, G. Marcos, T. Thiriet, S. Weber, and H. Michel, "Fundamental and Innovations in Plasma Assisted Diffusion of Nitrogen and Carbon in Austenitic Stainless Steels and Related Alloys," *Plasma Processes and Polymers* 6 (2009): 401–409, https://doi.org/10.1002/ppap.200930003.

44. M. Somers, Ö. Kücükyildiz, C. Ormstrup, et al., "Residual Stress in Expanded Austenite on Stainless Steel; Origin, Measurement, and Prediction," *Materials Performance and Characterization* 7 (2018): 693–716, https://doi.org/10.1520/MPC20170145.

45. Q. Luo and S. Yang, "From Micro to Nano Scales -Recent Progress in the Characterization of Nitrided Austenitic Stainless Steels," *International Journal of Nanomedicine and Nanosurgery* 1 (2015): 1, https://doi.org/10.16966/2470-3206.101.

46. M. G. Bolotov, G. P. Bolotov, and M. M. Rudenko, "The Impact of Nitriding Parameters on Evolution of Properties of Stainless-Steel Surface Plasma-Nitrided in Glow Discharge," *Progress in Physics of Metals* 25 (2024): 74–113.

47. R. P. Cardoso, M. Mafra, and S. F. Brunatto, "Low-Temperature Thermochemical Treatments of Stainless Steels – An Introduction," in *Plasma Science and Technology - Progress in Physical States and Chemical Reactions*, ed. T. Mieso (InTech, 2016), 107–130. ISBN 978-953-51-2280-7, https://doi.org/10.5772/61989.

48. A. P. Tschiptschin and C. E. Pinedo, "Surface Hardening of Stainless Steel," in *Stainless Steels*, ed. A. Singh (IntechOpen, 2022), 94–174. ISBN 978-1-80355-133-3, https://doi.org/10.5772/intechopen.105036.

49. H.-J. Spies, "Corrosion Behaviour of Nitrided, Nitrocarburised and Carburised Steels," in *Thermochemical Surface Engineering of Steel*, ed. E. J. Mittemeijer and M. A. J. Somers (Woodhead Publishing, 2015), 267–309. ISBN 978-0-85709-592-3, https://doi.org/10.1533/9780857096524.2.267.

50. L. Meijun, L. Xu, C. Zhu, Z. Li, and S. Wei, "Research Progress of High Entropy Alloy: Surface Treatment Improves Friction and Wear Properties," *Journal of Materials Research and Technology* 28 (2024): 752–773, https://doi.org/10.1016/j.jmrt.2023.12.011.

51. K. Ichii, K. Fujimura, and T. Takase, "Structure of the Ion-Nitrided Layer of 18-8 Stainless Steel," *Technology Reports of Kansai University* 27 (1986): 135–144.

52. F. Matsuda, K. Nakata, T. Makishi, and S. Kiya, "Surface Hardening of Ni Alloys by Means of Plasma Ion Nitriding (PIN) Process (Report II): Effect of Alloying Elements on Surface Hardening," *Transactions of JWRI* 17 (1988): 407–416, https://doi.org/10.18910/4220.

53. F. Borgioli, A. Fossati, E. Galvanetto, T. Bacci, and G. Pradelli, "Glow Discharge Nitriding of AISI 316L Austenitic Stainless Steel: Influence of Treatment Pressure," *Surface and Coatings Technology* 200 (2006): 5505–5513, https://doi.org/10.1016/j.surfcoat.2005.07.073.

54. T. Christiansen and M. A. J. Somers, "Controlled Dissolution of Colossal Quantities of Nitrogen in Stainless Steel," *Metallurgical and Materials Transactions A* 37 (2006): 675–682, https://doi.org/10.1007/s11661-006-0039-5.

55. T. L. Christiansen, K. Ståhl, B. K. Brink, and M. A. J. Somers, "On the Carbon Solubility in Expanded Austenite and Formation of Hägg Carbide in AISI 316 Stainless Steel," *Steel Research International* 87 (2016): 1395–1405, https://doi.org/10.1002/srin.201500415.

56. T. Czerwiec, H. He, A. Saker, et al., "Reactive Magnetron Sputtering as a Way to Improve the Knowledge of Metastable f.c.c. Nitrogen Solid Solutions Formed During Plasma Assisted Nitriding of Inconel 690," *Surface and Coatings Technology* 174–175 (2003): 131–138, https://doi.org/10.1016/S0257-8972(03)00529-2.

57. Z. Li, T. Paramasivam, W. Niu, et al., "Surface Engineering of IN-718 by Low-Temperature Carburisation: Properties and Thermal Stability," *Surface Engineering* 35 (2019): 281–293, https://doi.org/10.1080/02670844.2018.1501936.

58. O. Öztürk, M. Fidan, and S. Mändl, "MFM Imaging of Expanded Austenite Formed on 304 SS and CoCrMo Alloys," *Surface and Coatings Technology* 256 (2014): 15–22, https://doi.org/10.1016/j.surfcoat.2013.11.045.

59. J. Cassar, B. Mallia, A. Mazzonello, A. Karl, and J. Buhagiar, "Improved Tribocorrosion Resistance of a CoCrMo Implant Material by Carburising," *Lubricants* 6 (2018): 76, https://doi.org/10.3390/lubricants6030076.

60. X. Tao, Y. Yang, J. Qi, et al., "Active Screen Plasma Nitriding of a Si-Alloyed FeCrNi Medium Entropy Alloy: High Interstitial Absorption and an Anomalous Si-Induced Decomposition Mechanism in N-Expanded Austenite," *Applied Surface Science* 624 (2023): 157137, https://doi.org/10.1016/j.apsusc.2023.157137.

61. Y. Peng, H. Duan, Y. Feng, J. Gong, and M. A. J. Somers, "Surface Hardening of $Al_{0.1}$CoCrFeNi and $Al_{0.5}$CoCrFeNi High-Entropy Alloys by Low-Temperature Gaseous Carburization," *Intermetallics* 160 (2023): 107943, https://doi.org/10.1016/j.intermet.2023.107943.

62. H. A. Wriedt, N. A. Gokcen, and R. H. Nafziger, "The Fe-N (Iron-Nitrogen) System," *Bulletin of Alloy Phase Diagrams* 8 (1987): 355–377, https://doi.org/10.1007/BF02869273.

63. H. Okamoto, "The C-Fe (Carbon-Iron) System," *Journal of Phase Equilibria* 13 (1992): 543–565, https://doi.org/10.1007/BF02665767.

64. M. Fonović, A. Leineweber, and E. J. Mittemeijer, "Experimental Investigation and Thermodynamic Modeling of the Ni-Rich Part of the Ni-N Phase Diagram," *Metallurgical and Materials Transactions A* 45 (2014): 4863–4874, https://doi.org/10.1007/s11661-014-2440-9.

65. M. Singleton and P. Nash, "The C-Ni (Carbon-Nickel) System," *Bulletin of Alloy Phase Diagrams* 10 (1989): 121–126, https://doi.org/10.1007/BF02881419.

66. M. Widenmeyer, L. Shlyk, N. Becker, R. Dronskowski, E. Meissner, and R. Niewa, "Synthesis of Metastable Co_4N, Co_3N, Co_2N, and $CoO_{0.74}N_{0.24}$ From a Single Azide Precursor and Intermediates in $CoBr_2$ Ammonolysis," *European Journal of Inorganic Chemistry* 2016 (2016): 4792–4801, https://doi.org/10.1002/ejic.201600684.

67. K. Ishida and T. Nishizawa, "The C-Co (Carbon-Cobalt) System," *Journal of Phase Equilibria* 12 (1991): 417–424, https://doi.org/10.1007/BF02645959.

68. A. Leineweber, F. Lienert, S. Glock, et al., "X-Ray Diffraction Investigations on Gas Nitrided Nickel and Cobalt," *Zeitschrift für Kristallographie Proceedings* 1 (2011): 293–298, https://doi.org/10.1524/zkpr.2011.0044.

69. S. Bhattacharyya, "Iron Nitride Family at Reduced Dimensions: A Review of Their Synthesis Protocols and Structural and Magnetic Properties," *Journal of Physical Chemistry C* 119 (2015): 1601–1622, https://doi.org/10.1021/jp510606z.

70. A. Houari, S. F. Matar, and V. Eyert, "Electronic Structure and Magnetic Ordering of NiN and Ni_2N From First Principles," *Electronic Structure* 1 (2019): 15002, https://doi.org/10.1088/2516-1075/aae7f4.

71. X. Liu, H. Lu, M. He, et al., "The Preparation and Antiferromagnetic Properties of Epitaxial Rocksalt-Type CoN Films," *Journal of Alloys and Compounds* 582 (2014): 75–78, https://doi.org/10.1016/j.jallcom.2013.08.001.

72. W. Lengauer, "Nitrides: Transition Metal Solid-State Chemistry," in *Encyclopedia of Inorganic and Bioinorganic Chemistry*, ed. R. A. Scott (John Wiley & Sons, Ltd, 2015), 197–213, https://doi.org/10.1002/9781119951438.eibc0146.pub2.

73. X. Wu, X. Xu, Y. Jiang, et al., "Nitriding High Entropy Alloy Films: Opportunities and Challenges," *Surface and Coatings Technology* 476 (2024): 130157, https://doi.org/10.1016/j.surfcoat.2023.130157.

74. T. L. Christiansen and M. A. J. Somers, "Low-Temperature Gaseous Surface Hardening of Stainless Steel: The Current Status," *Zeitschrift für Metallforschung und Advanced Technology* 100 (2009): 1361–1377, https://doi.org/10.3139/146.110202.

75. X. Tao, X. Liu, A. Matthews, and A. Leyland, "The Influence of Stacking Fault Energy on Plasticity Mechanisms in Triode-Plasma Nitrided Austenitic Stainless Steels: Implications for the Structure and Stability of Nitrogen-Expanded Austenite," *Acta Materialia* 164 (2019): 60–75, https://doi.org/10.1016/j.actamat.2018.10.019.

76. X. Tao, J. Kavanagh, X. Li, H. Dong, A. Matthews, and A. Leyland, "An Investigation of Precipitation Strengthened Inconel 718 Superalloy After Triode Plasma Nitriding," *Surface and Coatings Technology* 442 (2022): 128401, https://doi.org/10.1016/j.surfcoat.2022.128401.

77. O. Öztürk, S. Okur, L. Pichon, M. O. Liedke, and J. P. Riviere, "Magnetic Layer Formation on Plasma Nitrided CoCrMo Alloy," *Surface and Coatings Technology* 205 (2011): S280–S285, https://doi.org/10.1016/j.surfcoat.2011.01.047.

78. H. L. Che and M. K. Lei, "Microstructure of Perfect Nitrogen-Expanded Austenite Formed by Unconstrained Nitriding," *Scripta Materialia* 194 (2021): 113705, https://doi.org/10.1016/j.scriptamat.2020.113705.

79. B. K. Brink, K. Ståhl, T. L. Christiansen, J. Oddershede, G. Winther, and M. A. J. Somers, "On the Elusive Crystal Structure of Expanded Austenite," *Scripta Materialia* 131 (2017): 59–62, https://doi.org/10.1016/j.scriptamat.2017.01.006.

80. T. L. Christiansen, T. S. Hummelshøj, and M. A. J. Somers, "Expanded Austenite, Crystallography and Residual Stress," *Surface Engineering* 26 (2010): 242–247, https://doi.org/10.1179/026708410X12506870724316.

81. T. Christiansen, K. V. Dahl, and M. A. J. Somers, "Nitrogen Diffusion and Nitrogen Depth Profiles in Expanded Austenite: Experimental Assessment, Numerical Simulation and Role of Stress," *Materials Science and Technology* 24 (2008): 159–167, https://doi.org/10.1179/026708307X232901.

82. Ö.C. Kücükyildiz, M. R. Sonne, J. Thorborg, M. A. J. Somers, and J. H. Hattel, "Thermo-Chemical-Mechanical Simulation of Low Temperature Nitriding of Austenitic Stainless Steel; Inverse Modelling of Surface Reaction Rates," *Surface and Coatings Technology* 381 (2020): 125145, https://doi.org/10.1016/j.surfcoat.2019.125145.

83. T. Moskaliovienė, P. Andriūnas, and A. Galdikas, "Coupled Modeling of Anisotropic Stress-Induced Diffusion and Trapping of Nitrogen in Austenitic Stainless Steel During Nitriding and Thermal Annealing," *Coatings* 13 (2023): 415, https://doi.org/10.3390/coatings13020415.

84. M. C. Conti, K. Andreas, W. Pierre Schembri, and J. Buhagiar, "Biocompatibility and Characterization of a Kolsterised® Medical Grade Cobalt-Chromium-Molybdenum Alloy," *Biomatter* 4 (2014): e27713, https://doi.org/10.4161/biom.27713.

85. Y. Peng, J. Gong, T. L. Christiansen, and M. A. J. Somers, "Surface Modification of CoCrFeNi High Entropy Alloy by Low-Temperature Gaseous Carburization," *Materials Letters* 283 (2021): 128896, https://doi.org/10.1016/j.matlet.2020.128896.

86. Y. Sun, "Hybrid Plasma Surface Alloying of Austenitic Stainless Steels With Nitrogen and Carbon," *Materials Science and Engineering: A* 404 (2005): 124–129, https://doi.org/10.1016/j.msea.2005.05.061.

87. J. Chen, X. Y. Li, T. Bell, and H. Dong, "Improving the Wear Properties of Stellite 21 Alloy by Plasma Surface Alloying With Carbon and Nitrogen," *Wear* 264 (2008): 157–165, https://doi.org/10.1016/j.wear.2006.12.012.

88. T. Lindner, M. Löbel, E. Saborowski, L.-M. Rymer, and T. Lampke, "Wear and Corrosion Behaviour of Supersaturated Surface Layers in the High-Entropy Alloy Systems CrMnFeCoNi and CrFeCoNi," *Crystals* 10 (2020): 110, https://doi.org/10.3390/cryst10020110.

89. E. L. Dalibón, S. M. Jafarpour, A. Dalke, H. Biermann, and S. P. Brühl, "Influence of Plasma Conditions and Surface Finish on Wear and Corrosion Behaviour of Nitrocarburized AISI 316 L," *Surface and Coatings Technology* 505 (2025): 132081, https://doi.org/10.1016/j.surfcoat.2025.132081.

90. K. Tong, F. Ye, H. Che, M. K. Lei, S. Miao, and C. Zhang, "High-Density Stacking Faults in a Supersaturated Nitrided Layer on Austenitic Stainless Steel," *Journal of Applied Crystallography* 49 (2016): 1967–1971, https://doi.org/10.1107/S1600576716014266.

91. F. A. P. Fernandes, T. L. Christiansen, G. Winther, and M. A. J. Somers, "Measurement and Tailoring of Residual Stress in Expanded Austenite on Austenitic Stainless Steel," *Materials Science and Engineering: A* 701 (2017): 167–173, https://doi.org/10.1016/j.msea.2017.06.082.

92. A. Maniee, F. Mahboubi, and R. Soleimani, "Improved Hardness, Wear and Corrosion Resistance of Inconel 718 Treated by Hot Wall Plasma Nitriding," *Metals and Materials International* 26 (2020): 1664–1670, https://doi.org/10.1007/s12540-019-00476-z.

93. Z. Ren, S. Eppell, S. Collins, and F. Ernst, "Co–Cr–Mo Alloys: Improved Wear Resistance Through Low-Temperature Gas-Phase Nitro-Carburization," *Surface and Coatings Technology* 378 (2019): 124943, https://doi.org/10.1016/j.surfcoat.2019.124943.

94. S. Tong, H. L. Che, and M. K. Lei, "High-Resolution TEM Characterization of Epitaxial Passivation for a High Nitrogen Face-Centered-Cubic Phase Formed on AISI 304L Austenitic Stainless Steel in Borate Buffer Solution," *Electrochimica Acta* 393 (2021): 139075, https://doi.org/10.1016/j.electacta.2021.139075.

95. A. H. Heuer, H. Kahn, F. Ernst, et al., "Enhanced Corrosion Resistance of Interstitially Hardened Stainless Steel: Implications of a Critical Passive Layer Thickness for Breakdown," *Acta Materialia* 60 (2012): 716–725, https://doi.org/10.1016/j.actamat.2011.10.004.

96. S. Tong, H. L. Che, K. S. Wang, and M. K. Lei, "Passivation Kinetics of a High Nitrogen Face-Centered-Cubic Phase Formed on AISI 304L Austenitic Stainless Steel in Borate Buffer Solutions by Photo- and Electrochemical Methods," *Electrochimica Acta* 394 (2021): 139110, https://doi.org/10.1016/j.electacta.2021.139110.

97. M. K. Lei and X. M. Zhu, "Role of Nitrogen in Pitting Corrosion Resistance of a High-Nitrogen Face-Centered-Cubic Phase Formed on Austenitic Stainless Steel," *Journal of the Electrochemical Society* 152 (2005): B291–B295, https://doi.org/10.1149/1.1939245.

98. X. M. Zhu and M. K. Lei, "Pitting Corrosion Resistance of High Nitrogen f.c.c. Phase in Plasma Source Ion Nitrided Austenitic Stainless Steel," *Surface and Coatings Technology* 131 (2000): 400–403, https://doi.org/10.1016/S0257-8972(00)00856-2.

99. Y. Sun, "Corrosion Behaviour of Low Temperature Plasma Carburised 316L Stainless Steel in Chloride Containing Solutions," *Corrosion Science* 52 (2010): 2661–2670, https://doi.org/10.1016/j.corsci.2010.04.017.

100. H. Y. Liu, H. L. Che, J. Y. Gao, G. B. Li, and M. K. Lei, "Low-Pressure Hollow Cathode Plasma Source Carburizing of AISI 304L Austenitic Stainless Steel at Low Temperature," *Surface and Coatings Technology* 442 (2022): 128548, https://doi.org/10.1016/j.surfcoat.2022.128548.

101. T. Li, S.-C. Chien, Z. Ren, W. Windl, F. Ernst, and G. S. Frankel, "Understanding the Efficacy of Concentrated Interstitial Carbon in Enhancing the Pitting Corrosion Resistance of Stainless Steel," *Acta Materialia* 221 (2021): 117433, https://doi.org/10.1016/j.actamat.2021.117433.

102. M. K. Lei, Z. L. Zhang, and X. M. Zhu, "Effects of Nitrogen-Induced Hcp Martensite Formation on Corrosion Resistance of Plasma Source Ion Nitrided Austenitic Stainless Steel," *Journal of Materials Science Letters* 18 (1999): 1537–1538, https://doi.org/10.1023/A:1006658820963.

103. Y. Sun, "Depth-Profiling Electrochemical Measurements of Low Temperature Plasma Carburised 316L Stainless Steel in 1M H_2SO_4 Solution," *Surface and Coatings Technology* 204 (2010): 2789–2796, https://doi.org/10.1016/j.surfcoat.2010.02.038.

104. D. Manova, S. Mändl, H. Neumann, and B. Rauschenbach, "Formation of Metastable Diffusion Layers in Cr-Containing Iron, Cobalt and Nickel Alloys After Nitrogen Insertion," *Surface and Coatings Technology* 312 (2017): 81–90, https://doi.org/10.1016/j.surfcoat.2016.09.059.

105. S. Mändl, H. Oh, D. Hristov, and D. Manova, "Stability of Expanded Austenite During Annealing in Vacuum," *Materials* 18 (2025): 546, https://doi.org/10.3390/ma18030546.

106. X. Y. Li, "Low Temperature Plasma Nitriding of 316 Stainless Steel – Nature of S Phase and Its Thermal Stability," *Surface Engineering* 17 (2001): 147–152, https://doi.org/10.1179/026708401101517746.

107. X. Y. Li, S. Thaiwatthana, H. Dong, and T. Bell, "Thermal Stability of Carbon S Phase in 316 Stainless Steel," *Surface Engineering* 18 (2002): 448–451, https://doi.org/10.1179/026708402225006259.

108. M. F. McGuire, *Stainless Steels for Design Engineers* (ASM International, 2008). ISBN 978-0-87170-717-8.

109. X. Tao, X. Li, H. Dong, A. Matthews, and A. Leyland, "Evaluation of the Sliding Wear and Corrosion Performance of Triode-Plasma Nitrided Fe-17Cr-20Mn-0.5N High-Manganese and Fe-19Cr-35Ni-1.2Si High-Nickel Austenitic Stainless Steels," *Surface and Coatings Technology* 409 (2021): 126890, https://doi.org/10.1016/j.surfcoat.2021.126890.

110. S. Lu, X. Zhao, S. Wang, J. Li, W. Wei, and J. Hu, "Performance Enhancement by Plasma Nitriding at Low Gas Pressure for 304 Austenitic Stainless Steel," *Vacuum* 145 (2017): 334–339, https://doi.org/10.1016/j.vacuum.2017.09.020.

111. P. Cisquini, S. V. Ramos, P. R. P. Viana, V. d. F. C. Lins, A. R. Franco, and E. A. Vieira, "Effect of the Roughness Produced by Plasma Nitrocarburizing on Corrosion Resistance of AISI 304 Austenitic Stainless Steel," *Journal of Materials Research and Technology* 8 (2019): 1897–1906, https://doi.org/10.1016/j.jmrt.2019.01.006.

112. F. Borgioli, E. Galvanetto, and T. Bacci, "Low Temperature Nitriding of AISI 300 and 200 Series Austenitic Stainless Steels," *Vacuum* 127 (2016): 51–60, https://doi.org/10.1016/j.vacuum.2016.02.009.

113. J. V. Sah, P. K. Dwivedi, S. Mukherjee, G. Jhala, and A. Joseph, "Influence of γ'_N and ε'_N Phases on the Properties of AISI 304L After Low-Temperature Plasma Nitrocarburizing," *Journal of Vacuum Science & Technology A* 41 (2023): 33101, https://doi.org/10.1116/6.0002346.

114. Y. Sun and T. Bell, "Sliding Wear Characteristics of Low Temperature Plasma Nitrided 316 Austenitic Stainless Steel," *Wear* 218 (1998): 34–42, https://doi.org/10.1016/S0043-1648(98)00199-9.

115. Z. Cheng, C. X. Li, H. Dong, and T. Bell, "Low Temperature Plasma Nitrocarburising of AISI 316 Austenitic Stainless Steel," *Surface and Coatings Technology* 191 (2005): 195–200, https://doi.org/10.1016/j.surfcoat.2004.03.004.

116. J. Buhagiar and H. Dong, "Corrosion Properties of S-Phase Layers Formed on Medical Grade Austenitic Stainless Steel," *Journal of Materials Science: Materials in Medicine* 23 (2012): 271–281, https://doi.org/10.1007/s10856-011-4516-z.

117. T. Czerwiec, H. He, S. Weber, C. Dong, and H. Michel, "On the Occurrence of Dual Diffusion Layers During Plasma-Assisted Nitriding of Austenitic Stainless Steel," *Surface and Coatings Technology* 200 (2006): 5289–5295, https://doi.org/10.1016/j.surfcoat.2005.06.014.

118. A. Fossati, F. Borgioli, E. Galvanetto, and T. Bacci, "Glow-Discharge Nitriding of AISI 316L Austenitic Stainless Steel: Influence of Treatment Time," *Surface and Coatings Technology* 200 (2006): 3511–3517, https://doi.org/10.1016/j.surfcoat.2004.10.122.

119. M. Martinesi, S. Bruni, M. Stio, C. Treves, T. Bacci, and F. Borgioli, "Biocompatibility Evaluation of Surface-Treated AISI 316L Austenitic Stainless Steel in Human Cell Cultures," *Journal of Biomedical Materials Research, Part A* 80 (2007): 131–145, https://doi.org/10.1002/jbm.a.30846.

120. A. Fossati, F. Borgioli, E. Galvanetto, and T. Bacci, "Corrosion Resistance Properties of Glow-Discharge Nitrided AISI 316L Austenitic Stainless Steel in NaCl Solutions," *Corrosion Science* 48 (2006): 1513–1527, https://doi.org/10.1016/j.corsci.2005.06.006.

121. D. S. Galeano-Osorio, S. Vargas, J. M. Vélez, A. Mello, M. N. Tanaka, and C. E. Castano, "Hemocompatibility of Plasma Nitrided 316L Stainless Steel: Effect of Processing Temperature," *Applied Surface Science* 509 (2019): 144704, https://doi.org/10.1016/j.apsusc.2019.144704.

122. M. C. S. Duarte, C. Godoy, and J. C. A.-B. Wilson, "Analysis of Sliding Wear Tests of Plasma Processed AISI 316L Steel," *Surface and Coatings Technology* 260 (2014): 316–325, https://doi.org/10.1016/j.surfcoat.2014.07.094.

123. T. Borowski, "Enhancing the Corrosion Resistance of Austenitic Steel Using Active Screen Plasma Nitriding and Nitrocarburising," *Materials* 14 (2021): 3320, https://doi.org/10.3390/ma14123320.

124. S. Adachi, M. Egawa, T. Yamaguchi, and N. Ueda, "Low-Temperature Plasma Nitriding for Austenitic Stainless Steel Layers With Various Nickel Contents Fabricated via Direct Laser Metal Deposition," *Coatings* 10 (2020): 365, https://doi.org/10.3390/coatings10040365.

125. S. Mändl and D. Manova, "Comparison of Nitriding Behavior for Austenitic Stainless Steel 316Ti and Super Austenitic Stainless Steel 904L," *Metals* 14 (2024): 659, https://doi.org/10.3390/met14060659.

126. F. Borgioli, E. Galvanetto, and T. Bacci, "Surface Modification of a Nickel-Free Austenitic Stainless Steel by Low-Temperature Nitriding," *Metals* 11 (2021): 1845, https://doi.org/10.3390/met11111845.

127. H. L. Che, S. Tong, K. S. Wang, M. K. Lei, and M. A. J. Somers, "Co-Existence of γ'_N Phase and γ_N Phase on Nitrided Austenitic Fe–Cr–Ni Alloys- I. Experiment," *Acta Materialia* 177 (2019): 35–45, https://doi.org/10.1016/j.actamat.2019.07.019.

128. D. L. Williamson, J. A. Davis, and P. J. Wilbur, "Effect of Austenitic Stainless Steel Composition on Low-Energy, High-Flux, Nitrogen Ion Beam Processing," *Surface and Coatings Technology* 103–104 (1998): 178–184, https://doi.org/10.1016/S0257-8972(98)00389-2.

129. I. S. Zhidkov, A. I. Kukharenko, A. V. Makarov, et al., "XPS Characterization of Surface Layers of Stainless Steel Nitrided in Electron Beam Plasma at Low Temperature," *Surface and Coatings Technology* 386 (2020): 125492, https://doi.org/10.1016/j.surfcoat.2020.125492.

130. J. Oddershede, T. L. Christiansen, K. Ståhl, and M. A. J. Somers, "Extended X-Ray Absorption Fine Structure Investigation of Nitrogen Stabilized Expanded Austenite," *Scripta Materialia* 62 (2010): 290–293, https://doi.org/10.1016/j.scriptamat.2009.11.021.

131. T. Bell, "Surface Engineering of Austenitic Stainless Steel," *Surface Engineering* 18 (2002): 415–422, https://doi.org/10.1179/026708402225006268.

132. L. J. O'Donnell, G. M. Michal, F. Ernst, H. Kahn, and A. H. Heuer, "Wear Maps for Low Temperature Carburised 316L Austenitic Stainless Steel Sliding Against Alumina," *Surface Engineering* 26 (2010): 284–292, https://doi.org/10.1179/026708410X12550773057901.

133. R. L. O. Basso, V. L. Pimentel, S. Weber, et al., "Magnetic and Structural Properties of Ion Nitrided Stainless Steel," *Journal of Applied Physics* 105 (2009): 124914, https://doi.org/10.1063/1.3153945.

134. X. Tao, A. Matthews, and A. Leyland, "On the Nitrogen-Induced Lattice Expansion of a Non-Stainless Austenitic Steel, Invar 36®, Under Triode Plasma Nitriding," *Metallurgical and Materials Transactions A* 51 (2019): 436, https://doi.org/10.1007/s11661-019-05526-0.

135. X. Tao, T. J. Collins, Q. Ao, et al., "Active Screen Plasma Nitriding of Fe-24Mn-2Al-0.45C TWIP Steel: Microstructure Evolution and a Synergistic Selective Oxidation Mechanism," *Acta Materialia* 241 (2022): 118418, https://doi.org/10.1016/j.actamat.2022.118418.

136. X. Yuan, Y. Zhao, X. Li, and L. Chen, "Effects of Gas Nitriding Temperature on the Surface Properties of a High Manganese TWIP Steel," *Metals* 7 (2017): 102, https://doi.org/10.3390/met7030102.

137. Z. Bai and X. Wu, "Improving Stress Corrosion Resistance and Wear Resistance of Austenitic Hot-Stamping Die Steels via Synergistic Effects of Shot Peening and Plasma Nitriding," *Surface and Coatings Technology* 478 (2024): 130448, https://doi.org/10.1016/j.surfcoat.2024.130448.

138. W. L. Mankins and S. Lamb, "Nickel and Nickel Alloys," in *ASM Handbook*, Vol. 2 (ASM International, 1990), 428–445. ISBN 978-1-62708-162-7, https://doi.org/10.31399/asm.hb.v02.a0001072.

139. H. S. Klapper, N. S. Zadorozne, and R. B. Rebak, "Localized Corrosion Characteristics of Nickel Alloys: A Review," *Acta Metallurgica Sinica (English Letters)* 30 (2017): 296–305, https://doi.org/10.1007/s40195-017-0553-z.

140. F. Pedraza, M. Reffass, G. Abrasonis, C. Savall, J. P. Rivière, and J. F. Dinhut, "Low-Energy High-Flux Nitriding of Ni and Ni20Cr Substrates," *Surface and Coatings Technology* 176 (2004): 236–242, https://doi.org/10.1016/S0257-8972(03)00735-7.

141. T. Makishi and K. Nakata, "Surface Hardening of Nickel Alloys by Means of Plasma Nitriding," *Metallurgical and Materials Transactions A* 35 (2004): 227–238, https://doi.org/10.1007/s11661-004-0123-7.

142. M. Fonović, A. Leineweber, O. Robach, E. A. Jägle, and E. J. Mittemeijer, "The Nature and Origin of "Double Expanded Austenite" in Ni-Based Ni-Ti Alloys Developing Upon Low Temperature Gaseous Nitriding," *Metallurgical and Materials Transactions A* 46 (2015): 4115–4131, https://doi.org/10.1007/s11661-015-2999-9.

143. D. Manova, D. Hirsch, J. W. Gerlach, S. Mändl, H. Neumann, and B. Rauschenbach, "In Situ Investigation of Phase Formation During Low Energy Ion Nitriding of Ni80Cr20 Alloy," *Surface and Coatings Technology* 259 (2014): 434–441, https://doi.org/10.1016/j.surfcoat.2014.10.054.

144. K. M. Eliasen, T. L. Christiansen, and M. A. J. Somers, "Low Temperature Gaseous Nitriding of Ni Based Superalloys," *Surface Engineering* 26 (2010): 248–255, https://doi.org/10.1179/026708409X12490360426043.

145. L. B. Varela, M. F. C. Ordoñez, C. E. Pinedo, and A. P. Tschiptschin, "Micro-Abrasive Wear Study of a Low-Temperature Plasma Nitrided Inconel 625 Superalloy," *Tribology: Materials, Surfaces & Interfaces* 16 (2022): 119–129, https://doi.org/10.1080/17515831.2021.1898899.

146. D. A. Skobir Balantič, Č. Donik, B. Podgornik, A. Kocijan, and M. Godec, "Improving the Surface Properties of Additive-Manufactured Inconel 625 by Plasma Nitriding," *Surface and Coatings Technology* 452 (2023): 129130, https://doi.org/10.1016/j.surfcoat.2022.129130.

147. C. Leroy, T. Czerwiec, C. Gabet, T. Belmonte, and H. Michel, "Plasma Assisted Nitriding of Inconel 690," *Surface and Coatings Technology* 142–144 (2001): 241–247, https://doi.org/10.1016/S0257-8972(01)01243-9.

148. Y. I. Oikava, B. C. E. S. Kurelo, G. Pintaude, V. T. Mazur, X. Li, and H. Dong, "The Effect of Counterbody Material on Tribological Behavior of Active Screen Plasma-Nitrided Inconel 718 Under Saline Solution," *Tribology Letters* 71 (2023): 116, https://doi.org/10.1007/s11249-023-01788-3.

149. Y. Nuñez de la Rosa, O. Palma Calabokis, V. Ballesteros-Ballesteros, C. L. Tafur, and P. C. Borges, "Assessment of the Pitting, Crevice Corrosion, and Mechanical Properties of Low-Temperature Plasma-Nitrided Inconel Alloy 718," *Metals* 13 (2023): 1172, https://doi.org/10.3390/met13071172.

150. Y. Jing, W. Jun, G. Tan, X. Ji, and F. Hongyuan, "Phase Transformations During Low Temperature Nitrided Inconel 718 Superalloy," *ISIJ International* 56 (2016): 1076–1082, https://doi.org/10.2355/isijinternational.ISIJINT-2015-697.

151. R. Sharghi-Moshtaghin, H. Kahn, Y. Ge, et al., "Low-Temperature Carburization of the Ni-Base Superalloy IN718: Improvements in Surface Hardness and Crevice Corrosion Resistance," *Metallurgical and Materials Transactions A* 41 (2010): 2022–2032, https://doi.org/10.1007/s11661-010-0299-y].

152. L. Pichon, J.-B. Dubois, S. Chollet, F. Larek, J. Cormier, and C. Templier, "Low Temperature Nitriding Behaviour of Ni_3Al-Like γ' Precipitates in Nickel-Based Superalloys," *Journal of Alloys and Compounds* 771 (2019): 176–186, https://doi.org/10.1016/j.jallcom.2018.08.187.

153. H. A. Wriedt, "The N-Ni (Nitrogen-Nickel) System," *Bulletin of Alloy Phase Diagrams* 6 (1985): 558–563.

154. A. Leineweber, F. Lienert, S. L. Shang, Z.-K. Liu, and E. J. Mittemeijer, "Ni_3N Compound Layers Produced by Gaseous Nitriding of Nickel Substrates; Layer Growth, Macrostresses and Intrinsic Elastic Anisotropy," *Journal of Materials Research* 27 (2012): 1531–1541, https://doi.org/10.1557/jmr.2012.40.

155. N. Pandey, M. Gupta, and J. Stahn, "Structure, Thermal Stability, and Magnetism of Ni_4N Thin Films," *Physica Status Solidi - Rapid Research Letters* 14 (2020): 2000294, https://doi.org/10.1002/pssr.202000294.

156. F. Matsuda, K. Nakata, and K. Tohmoto, "Ion Nitriding Hardening of Non Ferrous Alloys (Report I)," *Transactions of JWRI* 12 (1983): 271–276, https://doi.org/10.18910/8583.

157. D. A. DeAntonio, D. Duhl, T. Howston, and M. F. Rothman, "Heat Treating of Superalloys," in *ASM Handbook*, Vol. 4 (ASM International, 1991), 793–814. ISBN 0-87170-379-3.

158. R. Lawitzki, S. Hassan, L. Karge, et al., "Differentiation of γ'- and γ''- Precipitates in Inconel 718 by a Complementary Study With Small-Angle Neutron Scattering and Analytical Microscopy," *Acta Materialia* 163 (2019): 28–39, https://doi.org/10.1016/j.actamat.2018.10.014.

159. L.-Y. Hao, X.-Z. Wen, X.-W. Lei, W.-J. Yao, and N. Wang, "Distinct Nitriding Behaviors of γ and γ' Phases in Ni-Based Superalloys: A First-Principles Study," *Journal of Alloys and Compounds* 920 (2022): 165996, https://doi.org/10.1016/j.jallcom.2022.165996.

160. L. Hao, Y. Bai, Y. Liu, X. Lei, W. Yao, and N. Wang, "First-Principles Study on Effects of X (Ta, Ti, and W) on the Nitriding Behavior of γ'-Ni_3Al in Ni-Based Superalloys: From the Surface Adsorption and Diffusion of Nitrogen," *Applied Surface Science* 626 (2023): 157249, https://doi.org/10.1016/j.apsusc.2023.157249.

161. H. Kovací, H. Ghahramanzadeh ASL, Ç. Albayrak, A. Alsaran, and A. Çelik, "Effect of Plasma Nitriding Parameters on the Wear Resistance of Alloy Inconel 718," *Metal Science and Heat Treatment* 58 (2016): 470–474, https://doi.org/10.1007/s11041-016-0037-1.

162. A. I. Linnik, A. M. Prudnikov, R. V. Shalaev, et al., "V Magnetic Properties and Thermal Modification of Nanostructured Films of Nickel Nitrides," *Technical Physics Letters* 39 (2013): 143–146, https://doi.org/10.1134/S1063785013020119.

163. W. Yang, S. Rehman, X. Chu, Y. Hou, and S. Gao, "Transition Metal (Fe, Co and Ni) Carbide and Nitride Nanomaterials: Structure, Chemical Synthesis and Applications," *ChemNanoMat* 1 (2015): 376–398, https://doi.org/10.1002/cnma.201500073.

164. A. Saker, H. He, T. Czerwiec, et al., "Reactive Magnetron Sputtering of Inconel 690 by Ar–N_2 Plasma," *Thin Solid Films* 516 (2008): 1029–1036, https://doi.org/10.1016/j.tsf.2007.07.212.

165. M. Akhlaghi, R. Hock, J. Dallmann, et al., "Gaseous Nitriding of Co-10 at% and -15 at% Cr Alloys at 400°C and 450°C," *Journal of Alloys and Compounds* 907 (2022): 164535, https://doi.org/10.1016/j.jallcom.2022.164535.

166. J. Chen and H. Dong, "Corrosion and Corrosion Wear Behaviour of Plasma Carburised Stellite 21 Co–Cr Alloy," *Tribology: Materials, Surfaces & Interfaces* 3 (2009): 24–30, https://doi.org/10.1179/175158309X419043.

167. M. C. Romero, A. P. Tschiptschin, and C. Scandian, "Low Temperature Plasma Nitriding of a Co30Cr19Fe Alloy for Improving Cavitation Erosion Resistance," *Wear* 426–427 (2019): 581–588, https://doi.org/10.1016/j.wear.2019.01.019.

168. D. B. Oliveira, A. R. Franco, and A. C. Bozzi, "Influence of Low Temperature Plasma Carbonitriding on Cavitation Erosion Resistance of the Stellite 250 Alloy – a Preliminary Evaluation," *Wear* 476 (2021): 203653, https://doi.org/10.1016/j.wear.2021.203653.

169. J. Cassar, B. Mallia, A. Karl, and J. Buhagiar, "EIS of Carburised CoCrMo: Evolution of Parameters Characterising the Metal-Electrolyte Interface," *Surface and Coatings Technology* 292 (2016): 90–98, https://doi.org/10.1016/j.surfcoat.2016.03.033.

170. X. Y. Li, N. Habibi, T. Bell, and H. Dong, "Microstructural Characterisation of a Plasma Carburised Low Carbon Co–Cr Alloy," *Surface Engineering* 23 (2007): 45–51, https://doi.org/10.1179/174329407X161564.

171. X. Luo, X. Li, Y. Sun, and H. Dong, "Tribocorrosion Behavior of S-Phase Surface Engineered Medical Grade Co–Cr Alloy," *Wear* 302 (2013): 1615–1623, https://doi.org/10.1016/j.wear.2013.01.023.

172. K. Shukla, A. A. Sugumaran, I. Khan, A. P. Ehiasarian, and P. E. Hovsepian, "Low Pressure Plasma Nitrided CoCrMo Alloy Utilising HIPIMS Discharge for Biomedical Applications," *Journal of the Mechanical Behavior of Biomedical Materials* 111 (2020): 104004, https://doi.org/10.1016/j.jmbbm.2020.104004.

173. K. Shukla, Y. Purandare, A. Sugumaran, A. Ehiasarian, I. Khan, and P. Hovsepian, "Correlation Between the Microstructure and Corrosion Performance of the HIPIMS Nitrided Bio-Grade CoCrMo Alloy," *Journal of Alloys and Compounds* 879 (2021): 160429, https://doi.org/10.1016/j.jallcom.2021.160429.

174. J. Lutz, D. Manova, J. W. Gerlach, M. Stormer, and S. Mandl, "Interpretation of Glancing Angle and Bragg–Brentano XRD Measurements for CoCr Alloy and Austenitic Stainless Steel After PIII Nitriding," *IEEE Transactions on Plasma Science* 39 (2011): 3056–3060, https://doi.org/10.1109/TPS.2011.2160292.

175. S. Mändl, J. Lutz, C. Díaz, J. W. Gerlach, and J. A. García, "Influence of Reduced Current Density on Diffusion and Phase Formation During PIII Nitriding of Austenitic Stainless Steel and CoCr Alloys," *Surface and Coatings Technology* 239 (2014): 116–122, https://doi.org/10.1016/j.surfcoat.2013.11.029.

176. D. Manova and S. Mändl, "Nitrogen Transport in Expanded Austenite Formed in Stainless Steels and CoCr Base Alloys," *Materials Performance and Characterization* 6 (2017): 617–641, https://doi.org/10.1520/MPC20160081.

177. Y. Purandare, K. Shukla, A. Sugumaran, A. Ehiasarian, I. Khan, and P. Hovsepian, "Improving Tribocorrosion Resistance of a Medical Grade CoCrMo Alloy by the Novel HIPIMS Nitriding Technique," *Journal of Science: Advanced Materials and Devices* 8 (2023): 100570, https://doi.org/10.1016/j.jsamd.2023.100570.

178. R. Lizárraga, F. Pan, L. Bergqvist, E. Holmström, Z. Gercsi, and L. Vitos, "First Principles Theory of the hcp-fcc Phase Transition in Cobalt," *Scientific Reports* 7 (2017): 3778, https://doi.org/10.1038/s41598-017-03877-5.

179. E. P. George, D. Raabe, and R. O. Ritchie, "High-Entropy Alloys," *Nature Reviews Materials* 4 (2019): 515–534, https://doi.org/10.1038/s41578-019-0121-4.

180. F. D. C. Garcia Filho, R. O. Ritchie, M. A. Meyers, and S. N. Monteiro, "Cantor-Derived Medium-Entropy Alloys: Bridging the Gap Between Traditional Metallic and High-Entropy Alloys," *Journal of Materials Research and Technology* 17 (2022): 1868–1895, https://doi.org/10.1016/j.jmrt.2022.01.118.

181. E. G. Astafurova and S. Astafurov, "Nitrogen Alloying of the Multicomponent CoCrFeNiMn Alloy: Processing, Microstructure and Properties," *Letters on Materials* 14 (2024): 278–292: (Review), https://doi.org/10.48612/letters/2024-4-278-292.

182. R. Yang, D. Wang, D. Liu, H. Yang, and J. Qiao, "Ion Nitriding of a Face-Centered Cubic High-Entropy Alloy: Nitriding Kinetics, the Effect of Temperature and Contact Stress on Tribological Behavior," *Intermetallics* 172 (2024): 108392, https://doi.org/10.1016/j.intermet.2024.108392.

183. Y. Yang, X. Li, X. Tao, B. Cai, and H. Dong, "Active Screen Plasma Nitriding of $FeCrNiCoMo_{0.2}$ High Entropy Alloy for Combating Wear," *Journal of Materials Research and Technology* 35 (2025): 7282–7291, https://doi.org/10.1016/j.jmrt.2025.03.082.

184. A. Fujii and A. Nishimoto, "CoCrFeNiTi High-Entropy Sintered Alloy With Metal Screen Direct Current Plasma Nitriding," in *Proceedings of the 29th International Federation for Heat Treatment and Surface Engineering World Congress - IFHTSE 2024* (ASM International, 2024), 97–106, https://doi.org/10.31399/asm.cp.ifhtse2024p0097.

185. T. Karimoto and A. Nishimoto, "Plasma-Nitriding Properties of CoCrFeMnNi High-Entropy Alloys Produced by Spark Plasma Sintering," *Metals* 10 (2020): 761, https://doi.org/10.3390/met10060761.

186. Y. Wang, Y. You, M. Yan, et al., "The Effect of La on the Surface Properties of Plasma Nitrided CoCrCuFeNi High-Entropy Alloys at 440 Degrees Celsius," *Coatings* 14 (2024): 303, https://doi.org/10.3390/coatings14030303.

187. L. J. Zhang, Z. K. Jiang, M. D. Zhang, et al., "Effect of Solid Carburization on the Surface Microstructure and Mechanical Properties of the Equiatomic CoCrFeNi High-Entropy Alloy," *Journal of Alloys and Compounds* 769 (2018): 27–36, https://doi.org/10.1016/j.jallcom.2018.07.329.

188. J. Oddershede, T. L. Christiansen, K. Ståhl, and M. A. J. Somers, "EXAFS Investigation of Low Temperature Nitrided Stainless Steel," *Journal of Materials Science* 43 (2008): 5358–5367, https://doi.org/10.1007/s10853-008-2791-y].

189. E. Lewin, "Multi-Component and High-Entropy Nitride Coatings—A Promising Field in Need of a Novel Approach," *Journal of Applied Physics* 127 (2020): 160901, https://doi.org/10.1063/1.5144154.

190. E. Menéndez, J.-C. Stinville, C. Tromas, et al., "Out-of-Plane Magnetic Patterning on Austenitic Stainless Steels Using Plasma Nitriding," *Applied Physics Letters* 96 (2010): 242509, https://doi.org/10.1063/1.3453567.